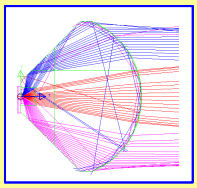

Ventura Photonics

Photonics Solutions

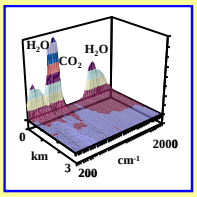

A REVIEW OF THE 1967 PAPER BY MANABE AND WETHERALD

S. Manabe and R. T. Wetherald (1967),

"Thermal equilibrium of the atmosphere with a given distribution of relative humidity"

***J. Atmos. Sci.* 24 pp. 241-249.**

[http://www.gfdl.noaa.gov/bibliography/related_files/sm6701.pdf]

Roy Clark PhD.

Ventura Photonics Climate Post 27, VPCP 027.1

Ventura Photonics

Thousand Oaks, CA

October 2023

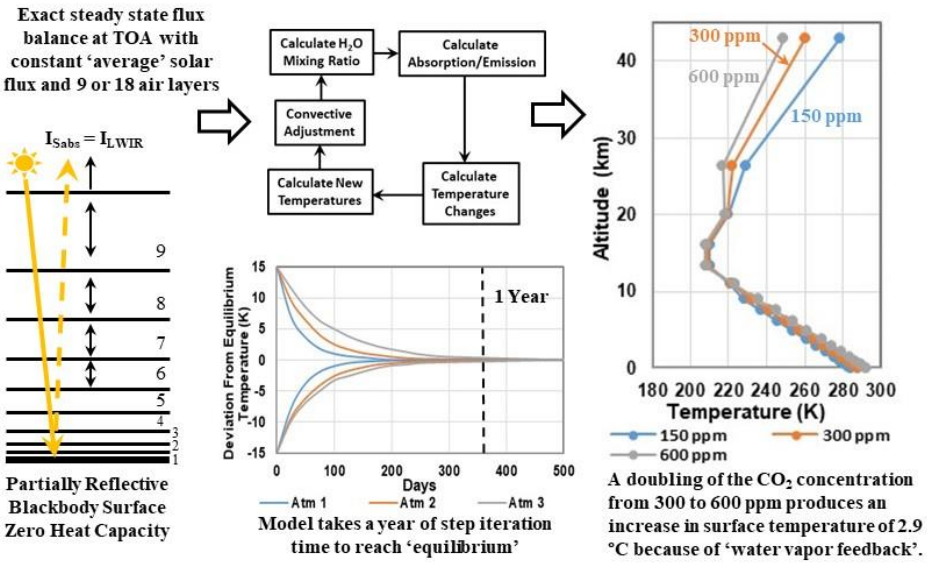

Table of Contents

Summary 3
Introduction 3
Historical Background 7
There is no Equilibrium or Steady State Climate 8
Temperatures at the Equator for the Moon and the Pacific Ocean 8
The El Niño Southern Oscillation and the Temperature of the Pacific Warm Pool 10
The Net Flux Balance at the Top of the Atmosphere 12
The MW67 Radiative Transfer Calculations 14
Molecular Line Broadening 16
LWIR Cooling Rates 18
The Dissipation of the Excess Heat in the Troposphere Produced by a CO_2 Doubling 22
The Coupling of the LWIR Flux to the Ocean Surface 25
The Coupling of the LWIR Flux to the Land Surface 28
The Fixed Relative Humidity Assumption and 'Water Vapor Feedback' 31
The Time Marching or Integration Error 37
Conclusions 39
Acknowledgement 39
References 39

Summary

The modern climate modeling fraud started with four papers, two by Manabe and Wetherald (M&W) in 1967 (MW67) and 1975 (MW75) and two by Hansen et al in 1976 (H76) and 1981 (H81). MW67 described a one dimensional radiative convective (1-D RC) model that provided the basic foundation for the climate modeling fraud. This model used the climate equilibrium assumption to oversimplify the climate energy transfer processes that determine the surface temperature. It was assumed that the time dependent flux terms could be replaced by average values. A 9 or 18 level radiative transfer model was used to calculate the rates of heating and cooling in the atmosphere. These were then used to derive the changes in temperature at each atmospheric level and recalculated at each step in an iterative process until the temperatures stabilized. The requirement for an exact energy balance at the top of the atmosphere between the absorbed solar flux and the long wave IR (LWIR) flux was then used to determine the steady state temperatures. When the CO_2 concentration was increased in this model, an increase in surface temperature was produced as a mathematical artifact of the calculation. In the real atmosphere, the change in the rates of tropospheric cooling produced by the change in CO_2 concentration are too small to detect in the normal day to day variation of the tropospheric temperatures. This was ignored by M&W. They allowed themselves to be trapped in the equilibrium climate 'box' and never validated their model. Furthermore, the initial temperature artifact was also amplified by a 'water vapor feedback' because of the fixed relative humidity distribution used in the model. M&W went on to incorporate their 1967 model artifacts into each unit cell of a 'highly simplified' global circulation model that was described in MW75. In H76 Hansen's group extended the mathematical artifacts created by CO_2 in MW67 to another 10 minor species N_2O, CH_4, NH_3, HNO_3, C_2H_4, SO_2, CH_3Cl, CCl_4, CF_2Cl_2 and $CFCl_3$. Then in H81 they added a 2 layer slab ocean and the step doubling CO_2 ritual and went on to use a contrived set of radiative forcings to simulate the global temperature record. This provided the pseudoscientific foundation for the radiative forcings, feedbacks and climate sensitivity still used by the climate modelers today.

The main focus of this article is a detailed review of the MW67 paper. However, the equilibrium assumption was introduced in the nineteenth century and important information is provided in earlier papers by Manabe's group. Also, in order to understand the errors in MW67, further explanation of the climate energy transfer processes and radiative transfer calculations is needed. Additional background information in these areas is provided as necessary.

Introduction

MW67 [Manabe and Wetherald, 1967] is a continuation of previous studies including Manabe and Strickler [1964] and Manabe and Möller [1961] where the primary objective was the "incorporation of radiative transfer into the general circulation model of the atmosphere". A radiative transfer calculation is used to provide a single static 'snapshot' of the atmospheric IR radiation field for the temperature and species concentration profiles specified. In MW67, the IR species were carbon dioxide, water vapor and ozone and the model had 9 or 18 atmospheric layers.

The heating effects of the solar radiation absorbed in the atmosphere by these species were also included. In addition, M&W imposed a fixed relative humidity distribution. Given the limited spectral data and the very limited computational resources available in 1967, the radiative transfer results for each calculation are quite good. Unfortunately, M&W chose to use the equilibrium climate assumption. They assumed that the time dependence of the flux terms could be replaced by average values and that there was an exact flux balance between the absorbed solar flux and the LWIR flux emitted at the top of their model atmosphere (TOMA). The ground surface in their model was a partially reflective blackbody with zero heat capacity. This was just a lower mathematical boundary to the radiative transfer calculation. The magnitude of lapse rate (tropospheric temperature profile) was constrained so as not exceed 6.5 K km^{-1}. The rates of solar heating and LWIR cooling determined by the radiative transfer algorithm were used in a series of iterative time steps to drive the model to a steady state condition where the absorbed solar flux was equal to the LWIR flux at TOMA. It required a year (number of time steps multiplied by the step interval) to reach steady state although the computational time was much less. M&W never addressed how such small changes in temperature could be detected in the normal daily and seasonal variations in temperature. Similarly, the temperature fluctuations in the turbulent boundary layer near the surface were not considered. The role of the oceans in setting the surface temperature was also neglected.

The set of assumptions used by M&W were clearly stated on the second page of their paper:

1) At the top of the atmosphere, the net incoming solar radiation should be equal to the net outgoing long wave radiation.
2) No temperature discontinuity should exist
3) Free and forced convection and mixing by the large scale eddies prevent the lapse rate from exceeding a critical lapse rate equal to 6.5 C km^{-1}.
4) Whenever the lapse rate is subcritical, the condition of local radiative equilibrium is satisfied.
5) The heat capacity of the earth's surface is zero.
6) The atmosphere maintains the given vertical distribution of relative humidity (new requirement).

Physical reality was abandoned in favor of mathematical simplicity. The MW67 model is illustrated in Figure 1.

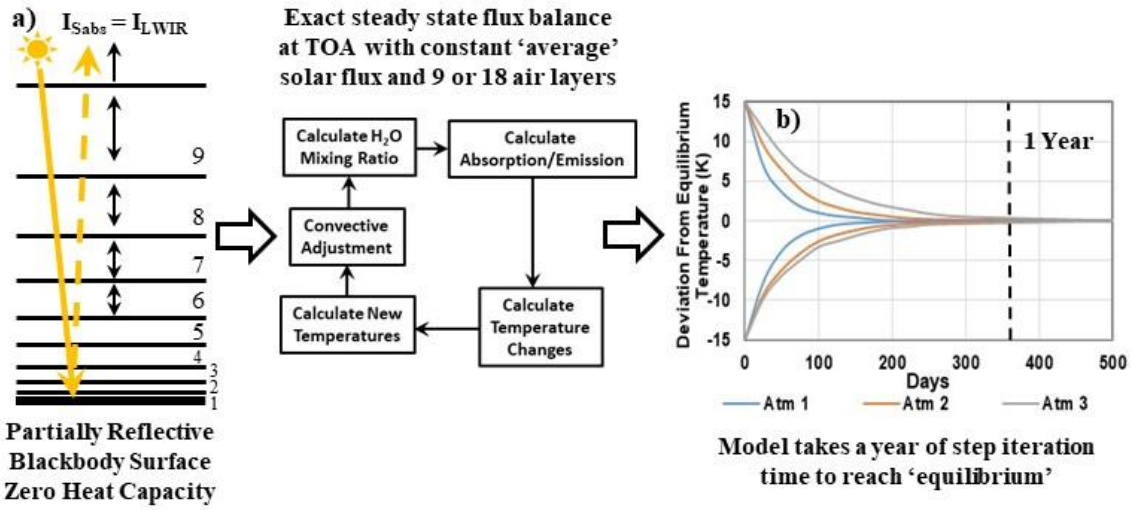

Figure 1: The 9 or 18 layer M&W model. It took a year of model time (number of steps multiplied by the step interval) to reach a steady state.

When the solar constant was changed, the MW67 model gave reasonable values for the surface temperature and the atmospheric temperature profile. This is shown in Figure 2a (MW67 figure 8). M&W used Langley (Ly) per minute for the flux units. (1 Ly is 1 calorie per cm^2 and 1 Ly per minute is close to 700 W m^{-2}). However, these results are just a single set of 'global average' numbers for each value of the solar constant. They have little physical meaning. When the CO_2 concentration was increased in the MW67 model, there was an initial decrease in the LWIR flux at TOMA. This was later called a radiative forcing [Ramaswamy et al, 2019]. The model was then run until a new equilibrium state was reached and the LWIR flux at TOMA was restored to its original value. As the temperature of the surface and air layers increased, the absolute water vapor concentration also increased because of the fixed relative humidity distribution used in the model. This produced an additional increase in the downward LWIR flux to the surface that amplified the initial temperature increase. There was also a decrease in temperature in the stratosphere. The effect of changing the CO_2 concentration in the MW67 model is illustrated in Figure 2b (MW67 figure16). The increase in surface temperature produced by the increase in CO_2 concentration was the expected result and M&W did not investigate any further. They made no attempt to validate their model using thermal engineering calculations of the surface temperature. They simply accepted the prevailing scientific dogma related to the equilibrium climate assumption. They never questioned their basic assumption that a simple 1-D RC steady state model could be used to describe the earth's climate. Their primary interest was developing a global circulation model (GCM) for climate studies. They were mathematicians not climate scientists.

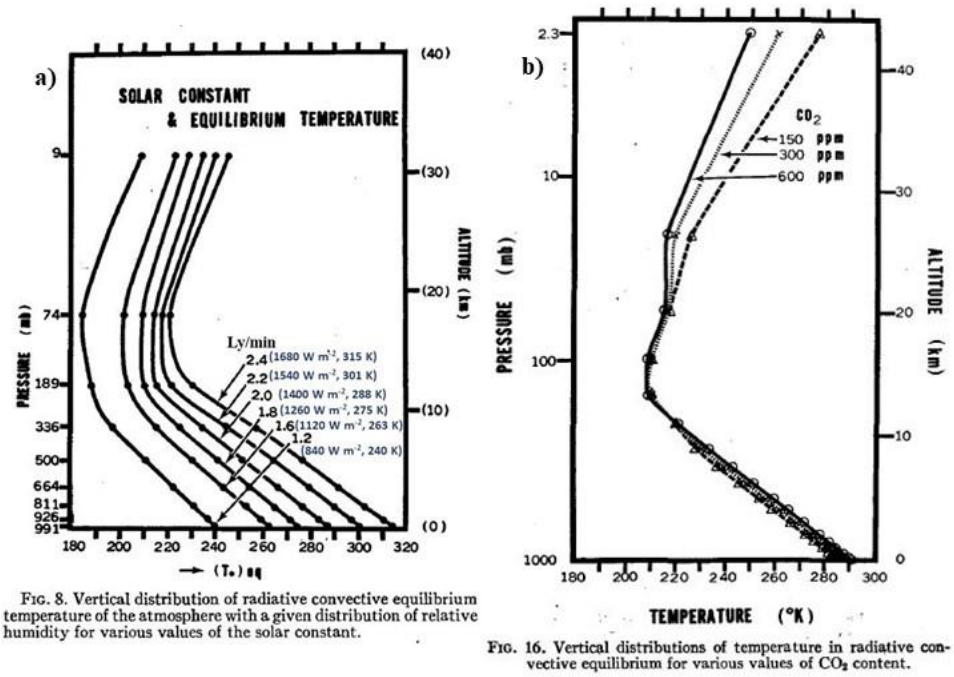

FIG. 8. Vertical distribution of radiative convective equilibrium temperature of the atmosphere with a given distribution of relative humidity for various values of the solar constant.

FIG. 16. Vertical distributions of temperature in radiative convective equilibrium for various values of CO_2 content.

Figure 2: a) Surface temperature and atmospheric temperature profiles for selected values of the solar constant, MW67, figure 8. The values of the solar constant in W m^{-2} and the surface temperatures are indicated in blue. b) The equilibrium temperature profiles calculated by the MW67 model for 150, 300 and 600 ppm CO_2 concentrations from MW67, figure 16.

M&W went on to incorporate their 1967 model artifacts into each unit cell of a 'highly simplified' global circulation model that was described in MW75 [Manabe and Wetherald, 1975]. In 1976, Hansen's group extended the mathematical artifacts created by CO_2 in MW67 to another 10 minor species (H76), [Wang et al, 1976]. Then in 1981 they added a 2 layer slab ocean and the step doubling CO_2 ritual and went on to use a contrived set of radiative forcings to simulate the global temperature record (H81), [Hansen et al, 1981]. The MW 67 model was simply copied without any attempt at model validation. The underlying assumptions were never questioned. This provided the pseudoscientific foundation for the radiative forcings, feedbacks and climate sensitivity still used by the climate modelers today [IPCC, AR6, WG1 Chapter 7, 2021].

There are six fundamental errors in MW67. First, there is no equilibrium average atmosphere. Second, the effects of molecular line broadening were ignored. Third, the change in the rate of cooling produced by a doubling of the CO_2 concentration from 300 to 600 pm is too small to have any measurable effect on the tropospheric temperature. Fourth, the increase in downward LWIR flux to the surface produced by a doubling of the CO_2 concentration cannot couple below the ocean surface and warm the oceans. Fifth, the day to day variation in the land surface temperature is sufficiently large that any increase surface temperature produced by a 'CO_2 doubling' cannot produce a measurable change in surface temperature. Sixth, the assumption of a fixed relative humidity distribution, especially near the surface is invalid. These errors will now be considered in more detail. However, the equilibrium assumption used by M&W was introduced in the nineteenth century, so a brief overview of the historical background will be provided first.

Historical Background

Fourier discussed the temperature of the earth in two similar memoires (reviews) in 1824 and 1827. An important and long neglected part of his discussion was the description of the seasonal time delays or phase shifts between the subsurface solar heating and the temperature response. Fourier was able to provide a quantitative analysis of these phase shifts using his theory of heat [Fourier, 1822]. This is clear evidence of a non-equilibrium thermal response to the solar flux. Similar phase shifts are found in the diurnal and seasonal temperature changes in both the land and ocean temperatures. This is discussed in more detail by Clark and Rörsch [2023] (CR23).

The equilibrium climate assumption was first introduced by Pouillet [1836]. It was assumed that the surface temperature could be explained using a steady state balance between the absorbed solar flux and the IR radiation. As a hypothesis, this had already been disproved by Fourier. Speculation that changes in the atmospheric concentration of CO_2 could cycle the earth through an Ice Age started with Tyndall [1861, 1863]. The first equilibrium air column model was introduced by Arrhenius [1896]. This had a fixed average solar flux, a partially reflective blackbody surface with zero heat capacity and a uniform air volume at a single temperature. Other energy transfer processes such as advection were assumed to be constant. When the CO_2 concentration was increased, there was an initial decrease in the LWIR flux emitted at the top of the model atmosphere (TOMA). The equilibrium constraint then requires that the surface temperature increase until the flux balance is restored at TOMA. This temperature increase is a mathematical artifact of the simplifications used in the model. Physical reality has been abandoned in favor of mathematical simplicity. Gradually, the idea that an increase in atmospheric CO_2 concentration could cause an increase in climate temperature became accepted as scientific dogma and the Ice Age cycle was replaced by concern over fossil fuel combustion.

One of the earliest uses of computers was for weather forecasting, pioneered by a group led by John von Neumann [Harper, 2004]. However, the global circulation models (GCMs) used in this application require the solution of large numbers of coupled nonlinear equations. Lorenz [1963, 1973] found that such solutions were unstable, even for a simple convection model with 3 equations. A practical limit for weather forecasting was 12 days ahead. This work should have made it clear that such GCMs have no predictive capabilities over the time scales associated with climate change.

The development of a computer climate model required two main steps. First, radiative transfer algorithms had to be improved so that the IR radiation field in the atmosphere, including the cooling rates could be calculated. Second, these algorithms had to be incorporated into each unit cell of a GCM modified for calculations over a climate time scale. A one dimensional (1-D) radiative equilibrium model was described by Manabe and Möller [1961] (MM61) and a 1-D RC model was described by Manabe and Strickler [1964] (MS64). However, the first generally accepted 1-D RC model was that of Manabe and Wetherald (MW67) [1967].

There is no Equilibrium or Steady State Climate

The use of the equilibrium assumption in climate science has led to a lot of confusion and can create warming as a mathematical artifact in the equilibrium climate models. A 24 hour average solar flux is a mathematical construct with little physical meaning. Temperatures at the lunar equator are close to equilibrium values. These are compared to those found along the equator in the Pacific Ocean to illustrate the differences in the energy transfer processes between the earth and the moon. The earth is a rotating water planet with an atmosphere that has an IR radiation field. The upward and downward LWIR fluxes at the surface combine to produce an exchange energy that limits the net LWIR cooling flux. The surface must warm so that the excess absorbed solar heat is removed by moist convection (evapotranspiration). The seasonal variation in the net flux at TOA also shows that the earth is not in equilibrium.

Temperatures at the Equator for the Moon and the Pacific Ocean

Thermal equilibrium means that there is an exact flux balance between the absorbed solar flux and LWIR flux emitted to space. The lunar surface under solar illumination is close to thermal equilibrium. The maximum temperature at the lunar equator at solar noon reaches 390 K (117 °C). There is almost no time delay or phase shift between the solar flux and the surface temperature response. At night the temperature cools to 93 K (-180 °C) and the change in temperature during a lunar day is near 297 K. The changes in temperature at the lunar equator are shown in Figure 3a and the related flux terms are shown in Figure 3b [CR23, Vasavada et al, 2012, Williams et al, 2017]. On the moon there is almost no atmosphere and the surface is powdered moon rock (regolith) with a very low thermal conductivity. Temperature control is provided by the Stefan Boltzmann Law. The LWIR cooling flux increases with the fourth power of the absolute temperature. During the day, the LWIR flux reaches a maximum near 1180 W m^{-2}. At night this decreases to approximately 4 W m^{-2} (CR23).

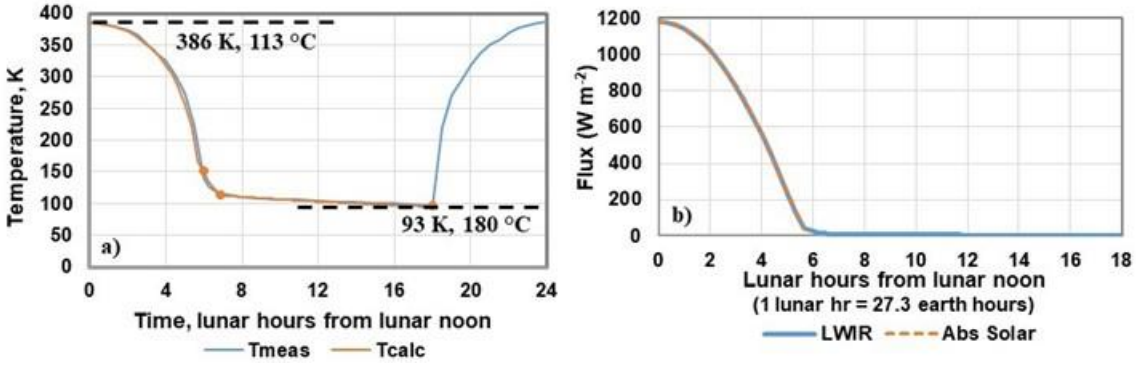

Figure 3: a) Measured and calculated lunar temperatures at the equator. For solar illumination from 0 to 6 hours, the temperature was calculated using the estimated blackbody emission produced by the absorbed solar flux. For the night time cooling, the blackbody emission was coupled to a surface thermal reservoir. b) The absorbed solar flux and the LWIR emission from the lunar surface (CR23).

Figure 4a shows the long term, 20 year (2000 to 2019) average of the daily temperatures and the one sigma standard deviations recorded by the TRITON buoy network along the equator in the

Pacific Ocean [CR23, TRITON, 2022]. The map shows the buoy locations in red. Figure 4b shows the related flux terms. The average temperature increases from 24±2.4 °C at 95° W to 30±0.4 °C at 147° E. The average solar flux decreases from 247 to 207 W m^{-2} and the net absorbed flux decreases from 160 to 45 W m^{-2}. Clearly, the energy transfer processes are very different from those on the moon. The earth is a rotating water planet with an atmosphere that has an IR radiation field. Over the oceans, the surface is almost transparent to the solar flux. Approximately 90% of this flux is initially absorbed within the first 10 m ocean layer. The large heat capacity of the ocean layers reduces the temperature rise. This stabilizes the earth's climate. At the surface, the downward LWIR flux from the lower troposphere to the surface establishes an exchange energy with the upward LWIR flux from the surface. The net upward cooling LWIR flux (upward minus downward LWIR flux) is limited to the emission into the atmospheric LWIR transmission window. The bulk ocean temperature increases until the water vapor pressure at the surface is sufficient for the excess solar heat to be removed by wind driven evaporation (latent heat flux). The heat is transported up through the troposphere by moist convection. This is a mass transport process. As the moist air rises through the troposphere it must interact with both the gravitational field and the angular momentum or rotation of the earth. This leads to the formation of the Hadley cell convective structure, the trade winds, the mid latitude cyclones/anticyclones and the ocean gyre circulation. The LWIR flux cannot be separated and analyzed independently of the other flux terms. It is an integral part of the energy transfer processes that determine the earth's weather patterns.

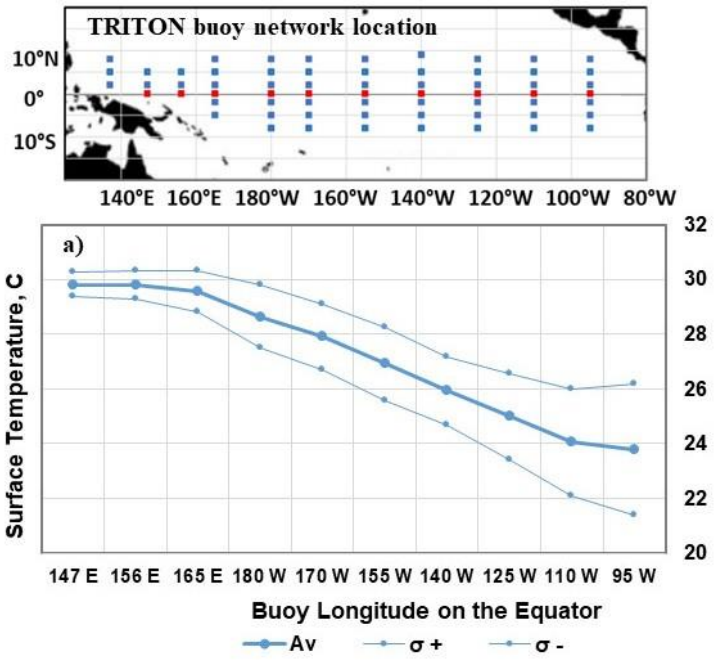

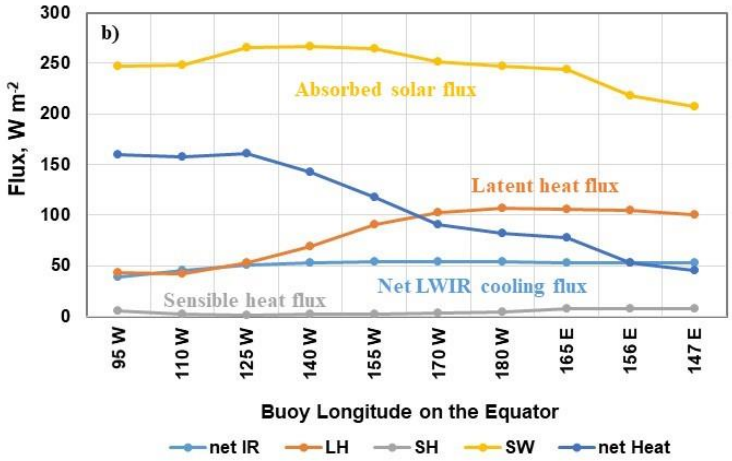

Figure 4: a) 20 year (2000 to 2019) average surface temperature and b) average flux terms for the TRITON buoys moored along the equator. The one sigma error margins are also plotted in a) for the surface temperatures.

The temperature increase from east to west is related to ocean transport by the Southern Equatorial Pacific Current. In the eastern equatorial Pacific Ocean, the wind driven evaporation is insufficient to remove all of the absorbed solar flux. The ocean water warms up as it is transported westwards by the equatorial current. This leads to the formation of the Pacific equatorial warm pool in the western equatorial Pacific Ocean. The solar flux decreases because of increased cloud cover and the latent heat flux increases as the surface temperature and the water vapor pressure increase. There is still a residual 50 W m^{-2} of net heat flux that is coupled into the warm pool. This is produced by shorter wavelength (green/blue) solar radiation that penetrates to lower depths and is not removed by the surface cooling.

The El Niño Southern Oscillation and the Temperature of the Pacific Warm Pool

There is no requirement for an exact flux balance between the absorbed solar flux and the ocean surface cooling. This also means that there is no exact flux balance at TOA. Any difference is accounted for by a change in the heat content of the oceans. This produces characteristic, quasi-periodic oscillations in ocean surface temperature that have major effects on the earth's climate. These oscillations are part of the ocean gyre circulation system. Variations in wind speed in the central equatorial Pacific Ocean interact with the equatorial currents to produce the El Niño Southern Oscillation (ENSO). As the wind speed decreases, both the ocean gyre current velocity and the latent heat flux decrease. This produces additional warming through an increase in transit time along the equatorial current and a decrease in the rate of evaporation. Conversely, an increase in wind speed produces cooling through both a decrease in transit time and an increase in the rate of evaporation. The wind speed is related to the Southern Oscillation Index, SOI which is a measure of the surface air pressure difference between Tahiti and Darwin, Australia. Figure 5 shows a plot of the monthly ENSO 3.4 index or temperature anomaly in the central equatorial Pacific Ocean. Overlaid on this is the SOI index, scaled to match the ENSO index [ENSO, 2022, SOI, 2022]. The scale factor is 0.086. The sign has also been reversed to match the ENSO index. The influence of the wind speed on the ENSO index is clear from the overlap of the two plots. The

temperature changes related to the ENSO are not limited to the surface temperature. They extend to depths of 75 to 100 m below the surface. This is discussed in more detail in CR23. These temperature changes have no relationship to any observed increase in the atmospheric concentration of CO_2.

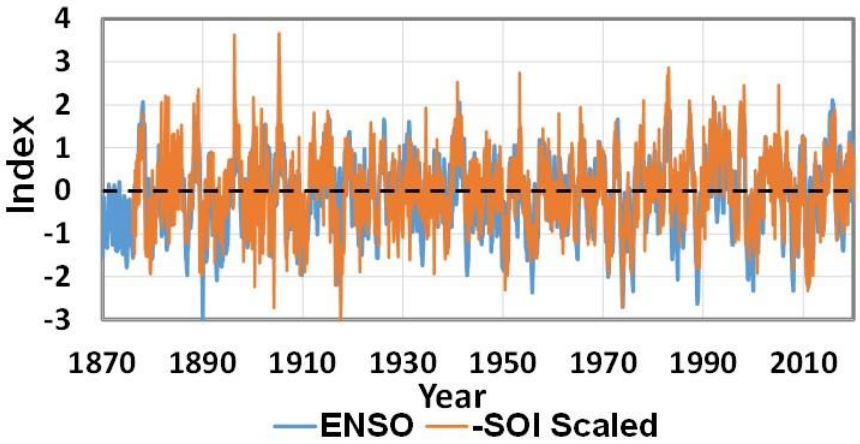

Figure 5: Monthly ENSO data series from 1870 plotted with the scaled SOI index from 1876. The SOI is multiplied by 0.086 and the sign is reversed to match the ENSO response.

In addition, the upper limit to tropical ocean surface temperatures is near 30 °C. When the surface temperature starts to increase above this, strong local thunderstorms are formed that limit the temperature rise [Eschenbach, 2010]. The changes in temperature related to the ENSO are produced by changes in the location and the area of the warm pool. There are also major changes in evaporation and precipitation patterns. The maximum ocean surface temperature does not increase. In addition, as the ENSO index increases, the temperatures in the lower troposphere also increase, with a time delay of a few months. The ENSO related changes in area of the equatorial Pacific Ocean warm pool are shown in Figures 6a and 6c [NRL, 2021]. The monthly ENSO index from 2019 and the UAH global lower tropospheric (tlt) temperature anomalies are shown in Figure 6b [UAH. 2022].

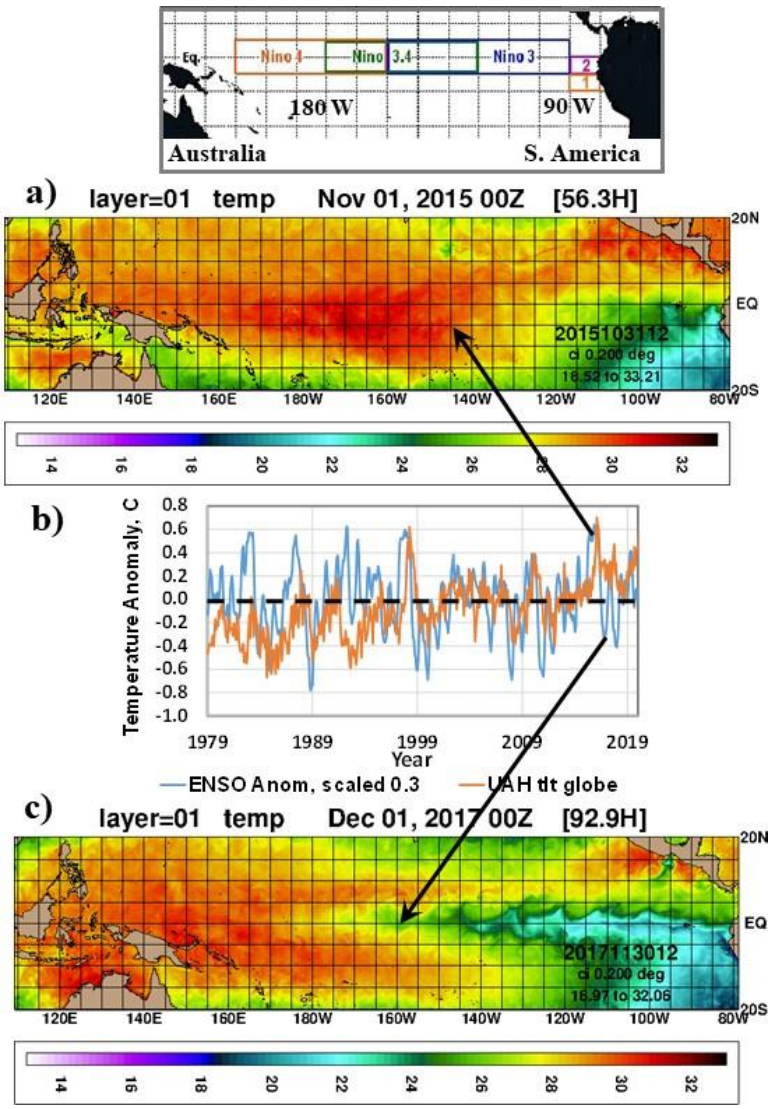

Figure 6: Surface temperatures in the equatorial Pacific Ocean for November 1, 2015 and December 1, 2017 corresponding to a) high and c) low values of the ENSO index. The map inset indicates the Nino 3.4 region used to determine the ENSO index. The monthly ENSO index and the UAH global lower tropospheric temperature anomaly (tlt) from satellite microwave measurements are shown in b).

The Net Flux Balance at the Top of the Atmosphere

Figure 7 shows the zonal average of the net flux at different latitudes (absorbed solar flux minus LWIR flux at the top of the atmosphere) for March, June, September and December [Kandel and Voilier, 2010]. Near equinox, in March and September, the net flux is positive with a net energy flow of up to 100 W m^{-2} into the atmosphere within the ±30° latitude bands. There is net cooling at higher latitudes. In June, near summer solstice in the N. Hemisphere, the heating occurs in the N. Hemisphere and this reverses in December for the S. Hemisphere summer. Figure 8 shows maps of the monthly average of the net flux for March, June, September and December 2000 recorded using the CERES instrument on the NASA Terra satellite. This illustrates the seasonal shift in solar heating (orange/red band) [CERES, 2004].

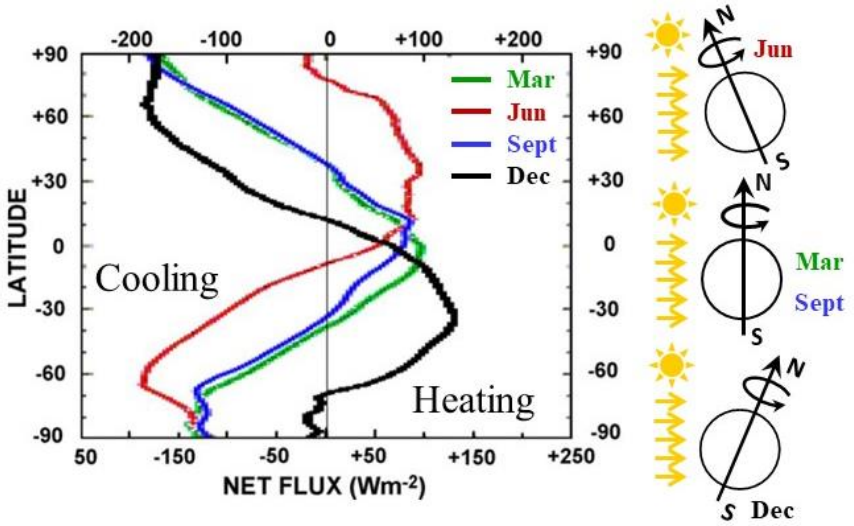

Figure 7: Zonal averages of the net flux (absorbed solar minus emitted LWIR flux), for March, June, September and December, five year average CERES values.

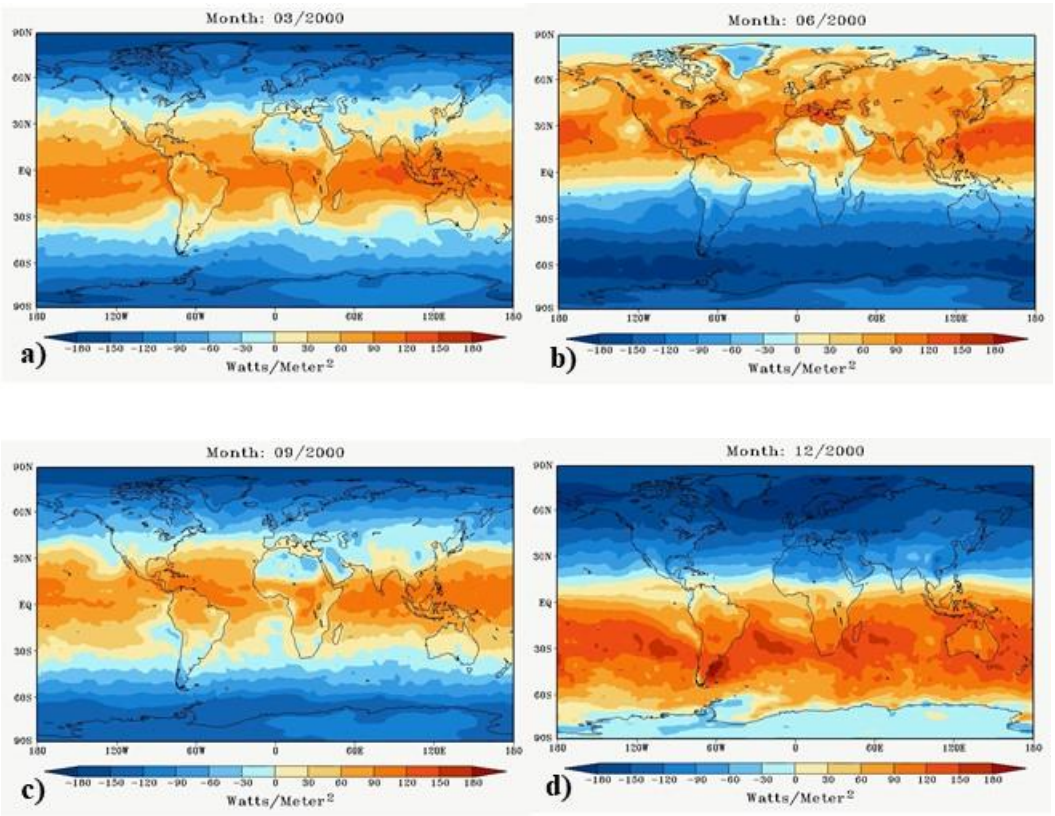

Figure 8: Spatially resolved CERES Terra monthly average net radiation balance at TOA for March, June, September and December 2000.

The concept of an energy balance for the earth is a contrived average obtained by integrating satellite radiometry data over both hemispheres. The requirement for climate stability is that the

thermal and/or humidity gradient at the surface dissipate the absorbed solar flux so as to maintain the surface temperature within the relatively narrow bounds needed to sustain life. This follows from the Second Law of Thermodynamics, not the First. As the surface temperatures change, the thermal gradients adjust. There is an approximate planetary energy balance between the absorbed solar flux and the LWIR flux returned to space at TOA. A change in surface temperature can change the LWIR flux emitted to space, but a change in LWIR flux produced by an increase in atmospheric greenhouse gas concentration does not change the surface temperature. The tail does not wag the dog.

The MW67 Radiative Transfer Calculations

MW67 used a 9 or 18 layer radiative transfer model. The levels used are shown in Figure 9. Simple absorption models based on measured wideband absorption data were used in the calculations as described in MW67 and MS64. At the time, high resolution molecular data were sparse and computer capabilities were very limited. However, the results for the calculation of the outgoing longwave radiation (OLR) are similar to measured data from Koll and Cronin [2018]. Figure 10a shows the calculation of the OLR from MW67 figure 10 and Figure 10b shows measured clear sky satellite data. The OLR in both cases shows a linear response to the surface temperature and magnitudes of the OLR are similar as indicated by the red asterisks. However, the emission by the water bands is determined in part by the local tropospheric temperature and the altitude of the emission increases with increasing surface temperature. Heat is stored as gravitational potential energy. LWIR emission from the surface to space is limited to the transmission through the atmospheric LWIR transmission window. Figure 11a shows the calculation of the net LWIR cooling flux from the surface vs. surface temperature from MW67 figure 14 and Figure 11b shows the same calculations from MODTRAN calculations using the tropical, mid latitude summer (MLS) and mid latitude winter (MLW) options [MODTRAN, 2023]. Here, the MW67 results are similar in magnitude to MODTRAN, but show the opposite trend and decrease with increasing temperature.

TABLE 10. Illustration of the 18-level σ-coordinate system based on $p_s = 1000$ mb. H denotes the approximate height of the level, and Δp is the pressure thickness of the layer.

Level	σ	p (mb)	Δp (mb)	H (km)
1	0.0277	2	9	42.9
2	0.0833	20	25	26.4
3	0.1388	53	40	20.1
4	0.1944	99	52	16.1
5	0.2500	156	62	13.3
6	0.3055	223	71	11.0
7	0.3611	297	77	9.0
8	0.4166	376	81	7.5
9	0.4722	458	83	6.1
10	0.5277	542	83	4.9
11	0.5833	624	81	3.7
12	0.6388	703	77	2.9
13	0.6944	777	71	2.1
14	0.7500	844	62	1.4
15	0.8055	901	52	0.86
16	0.8611	947	40	0.46
17	0.9166	980	25	0.18
18	0.9722	998	9	0.02

TABLE 11. Illustration of the 9-level σ-coordinate system based on $p_s = 1000$ mb.

Level	σ	p (mb)	Δp (mb)	H (km)
1	0.0555	9	34	31.6
2	0.1666	74	92	18.0
3	0.2777	189	133	12.0
4	0.3888	336	158	8.3
5	0.4999	500	166	5.5
6	0.6110	664	158	3.3
7	0.7221	811	133	1.7
8	0.8332	926	92	0.64
9	0.9443	991	34	0.07

Definition of σ

$$p/p_0 = \sigma^2(3\text{-}2\,\sigma)$$

P = atmospheric pressure

P_0 = 1000 mb

Figure 9: The levels used in the 9 or 18 level MW67 radiative transfer model

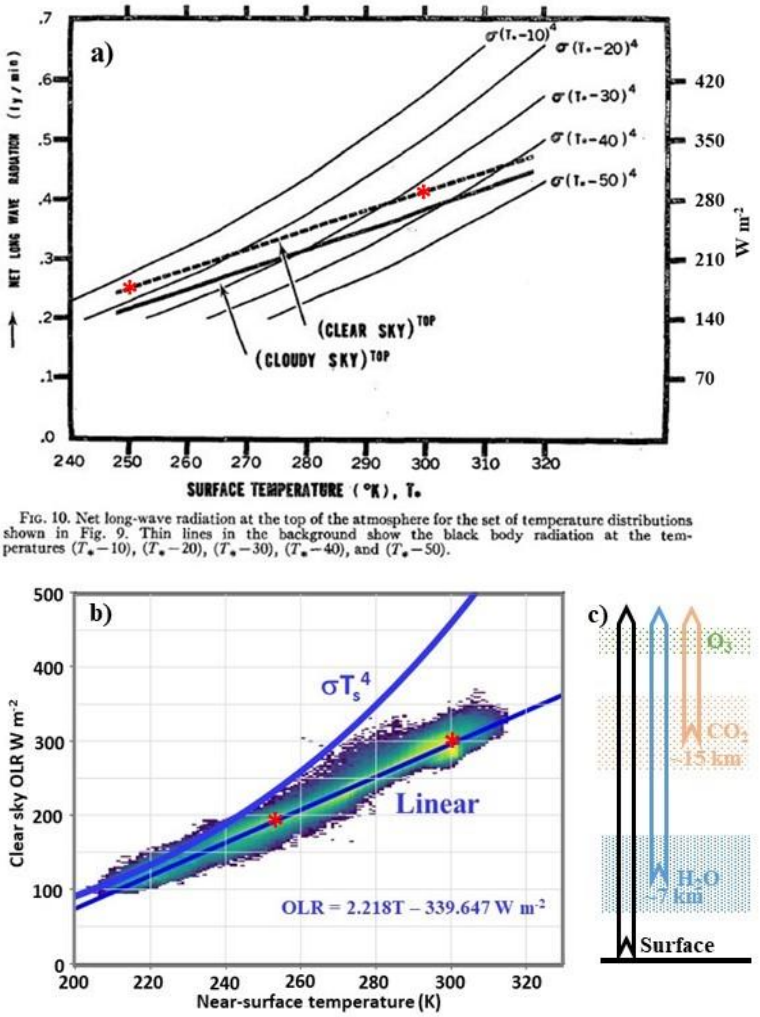

FIG. 10. Net long-wave radiation at the top of the atmosphere for the set of temperature distributions shown in Fig. 9. Thin lines in the background show the black body radiation at the temperatures (T_s-10), (T_s-20), (T_s-30), (T_s-40), and (T_s-50).

Figure 10: a) OLR vs. surface temperature from MW67, b) satellite data from Koll and Cronin [2018] and c) emission levels (schematic).

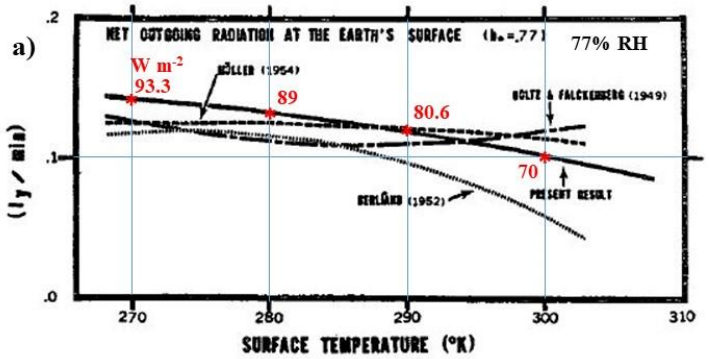

FIG. 14. Values of net upward long-wave radiation at the earth's surface which are computed from the empirical formulas obtained by various authors as well as the values from the present contribution.

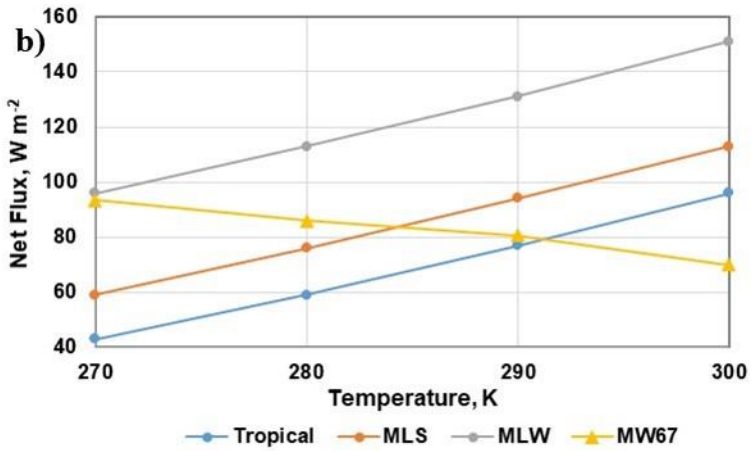

Figure 11: a) Net upward LWIR cooling flux emitted by the surface vs. surface temperature from MW67 figure 14 and b) the corresponding values from MODTRAN calculations for three different atmospheric profiles.

Molecular Line Broadening

The atmospheric LWIR flux consists of IR emission and absorption from many overlapping lines. Each line is a specific transition between two molecular rotation-vibration states. The line positions and linestrengths for H_2O, CO_2, O_3, N_2O and CH_4 are shown in Figure 12 [Wijngaarden, and Happer, 2022]. The main atmospheric CO_2 bands of interest are circled in red. The lines are broadened by molecular collisions. Near the surface within the main absorption emission bands, the lines overlap and merge into a quasi-continuum. At higher altitudes, these lines become narrower as the temperature and pressure decrease. Some of the upward LWIR flux can pass through the gaps between these narrower lines above and continue to space without additional absorption/emission. The downward flux is absorbed by the broader lines below. This is illustrated schematically in Figure 13a for a single line and in Figure 13b for a group of lines in the 590 to 600 cm^{-1} region. Almost all of the downward LWIR flux that reaches the surface originates from within the first 2 km layer of the troposphere. Approximately half of this downward flux originates from the first 100 m layer. This is shown in Figure 13c [Clark, 2013]. The downward LWIR flux to the surface is therefore decoupled from the LWIR emission to space. When the CO_2 concentration is increased, the small amount of additional heat that is released into the troposphere cannot couple to the surface. Instead it is re-radiated to space by wideband LWIR emission.

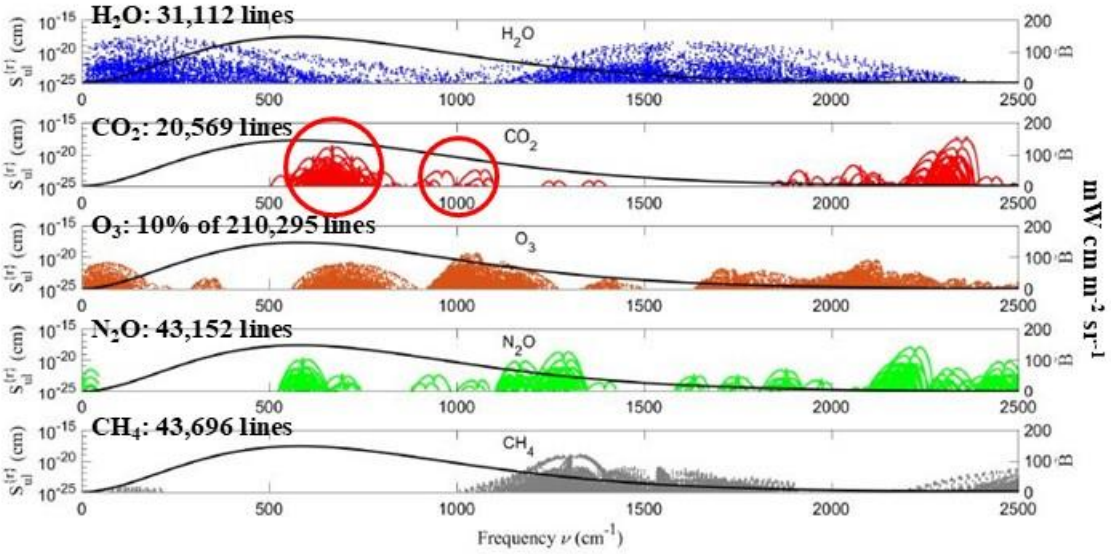

Figure 12: HITRAN linestrengths at 296 K for H_2O, CO_2, O_3, N_2O and O_3 plotted vs. wavenumber from 0 to 2500 cm^{-1}. The smooth black line is the blackbody emission at 296 K. The number of lines plotted are indicated for each species. Because of the large number of lines, only 10% of the O_3 lines, selected randomly, are plotted. The main atmospheric absorption bands of interest for CO_2 are circled in red.

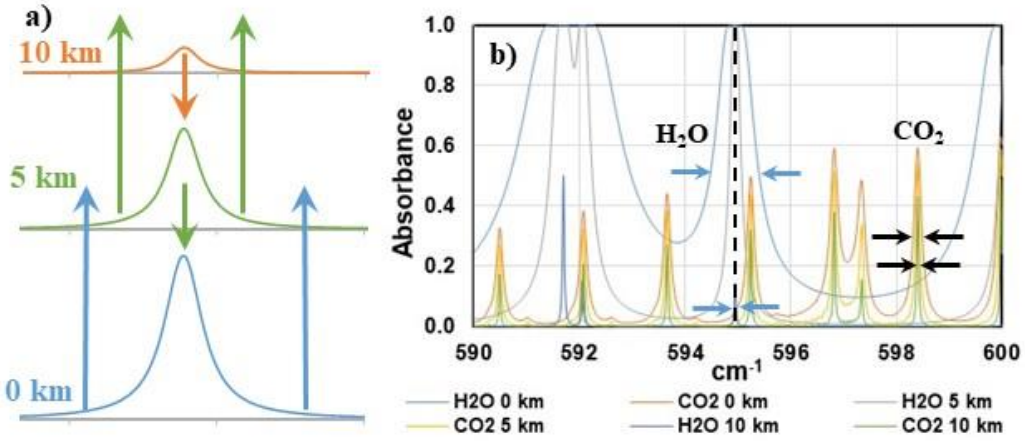

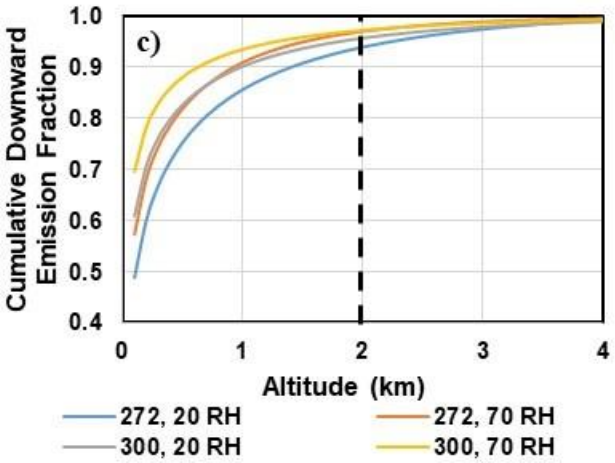

Figure 13: a) Transition from absorption-emission to free photon flux as the linewidth decreases with altitude. Single H_2O line near 231 cm^{-1}. b) Linewidths for H_2O and CO_2 lines in the 590 to 600 cm^{-1} spectral region for altitudes of 0, 5 and 10 km. c) Cumulative fraction of the downward flux at the surface vs. altitude for surface temperatures of 272 and 300 K, each with 20 and 70% relative humidity (RH). Almost all of the downward flux reaching the surface originates from within the first 2 km layer. This is the location of the lower tropospheric reservoir.

LWIR Cooling Rates

M&W made the invalid assumption that the surface temperature could be determined using a steady state flux model based on a mathematical average of the incident solar flux and a similar average of the OLR at TOA. In the real world, there is no steady state. The solar insolation changes on both daily and seasonal time scales. The peak solar flux with the sun close to zenith (overhead) is near 1000 W m^{-2}. At night and during polar winter it is zero. The surface temperature is determined by the interactive flux terms at the surface-air interface coupled to the surface thermal reservoir. This is discussed in detail in CR23. There are also significant time delays or phase shifts between the peak solar flux and the surface temperature response as heat is transferred into the surface thermal reservoirs. In order to understand the thermal properties of the atmosphere, the radiative transfer calculations have to be extended to include the cooling rates and the change in the cooling rates as the CO_2 concentration or that of other greenhouse gases is changed. In addition, an air parcel in the lower troposphere is part of the turbulent convective boundary layer. As the air parcel changes altitude, the temperature changes because of expansion and contraction with the changes in pressure. These temperature changes are larger than those produced by any change in the LWIR cooling rate related to an increase in greenhouse gas concentration.

The determination of LWIR cooling rates is well understood. The net LWIR flux at each level in the radiative transfer calculation is divided by the local heat capacity. The cooling rates for CO_2 were discussed by Plass [1956] and the cooling rates for CO_2, H_2O and O_3 were discussed by Manabe and Strickler [1964]. This is illustrated in Figure 14. After the publication of MW67, cooling rates were discussed by Stone and Manabe [1968] (SM68) and by Ackerman [1979], as shown in Figures 15a and 15b. Ackerman also discussed the change in the rate of cooling for an increase in CO_2 concentration from 300 to 600 ppm as shown in Figures 15c and 15d. The cooling

rates for H_2O, CO_2, O_3, CH_4 and N_2O were discussed by Lacis and Oinas [1991]. This is shown in Figure 16. More recent calculations have been published by Feldman et al [2008] and by Iacono et al [2008]. Figure 17a shows the LWIR emission spectrum at TOA for 0, 400 and 800 ppm CO_2 concentrations from Wijngaarden, and Happer [2022]. Figure 17b shows the CO_2 emission band on an enlarged scale. Figure 17c shows the change in the LWIR flux as the CO_2 concentration is changed from 400 to 800 ppm. Figure 17d shows the total (10 to 3250 cm^{-1}) and band-averaged IR cooling rate profiles for the tropical model atmosphere on a log-pressure scale [Feldman et al, 2008]. The tropospheric cooling rate varies between 2 and 2.5 K per day (light blue line). Figure 17e shows the change in the total tropospheric LWIR cooling rate for a CO_2 doubling, in this case from approximately 300 to 600 ppm. There is a maximum change in the cooling rate of +0.08 K per day. At a lapse rate of -6.5 K km^{-1}, an increase in temperature of +0.08 K is produced by a decrease in altitude of 12 meters. This is equivalent to riding an elevator down four floors. At higher altitudes in the stratosphere, near 50 km, this increase in CO_2 concentration produces an increase in the cooling rate approximately 3 K per day as shown in Figure 17f. However, the air density here is low, 1 mb or 0.001 atm., so the change LWIR flux is small, near -40 μW m^{-2}. In addition, these changes in flux do not couple downwards into the lower troposphere because of line broadening effects at lower altitudes. In spite of an extensive discussion of the LWIR cooling rates, a fundamental error in the 1-D RC model was ignored. When the atmospheric concentration of a greenhouse gas such as CO_2 is increased, the change in the rate of cooling in the troposphere is too small to measure. Any additional heat released into the lower troposphere is coupled to the normal motion of the turbulent boundary layer and dissipated by wideband LWIR emission. This is illustrated in Figure 18b below. While the LWIR cooling rates were discussed in MS64 and SM68, there was no consideration of the changes in the rates of cooling produced by a doubling of the CO_2 concentration.

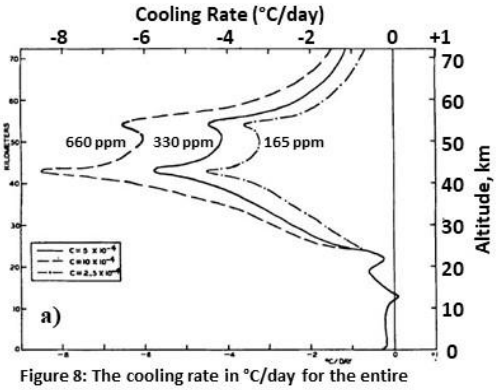

Figure 8: The cooling rate in °C/day for the entire frequency interval from 12μ-18 μ. Curves are given for the following CO_2 concentrations: c = 5 x 10^{-4} (0.033% by volume); c = 10 x 10^{-4} (0.066% by volume); c = 2.5 x 10^{-4} (0.0165% by volume). There is no difference in the cooling rates below 24 km.

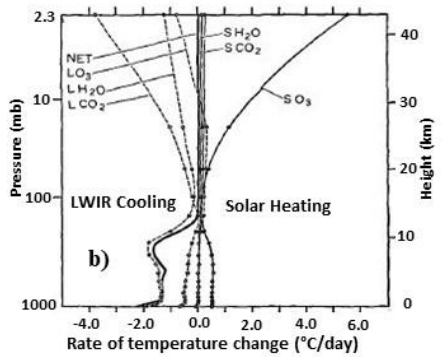

Figure 8c: Vertical distribution of the radiative heat balance components for the thermal equilibrium of a clear atmosphere

Figure 14: a) Cooling rates for CO_2 at atmospheric concentrations of 660, 330 and 165 ppm [Plass, 1956] and b) LWIR cooling rates and solar heating rates for CO_2, H_2O and O_3 [Manabe and Strickland, 1964].

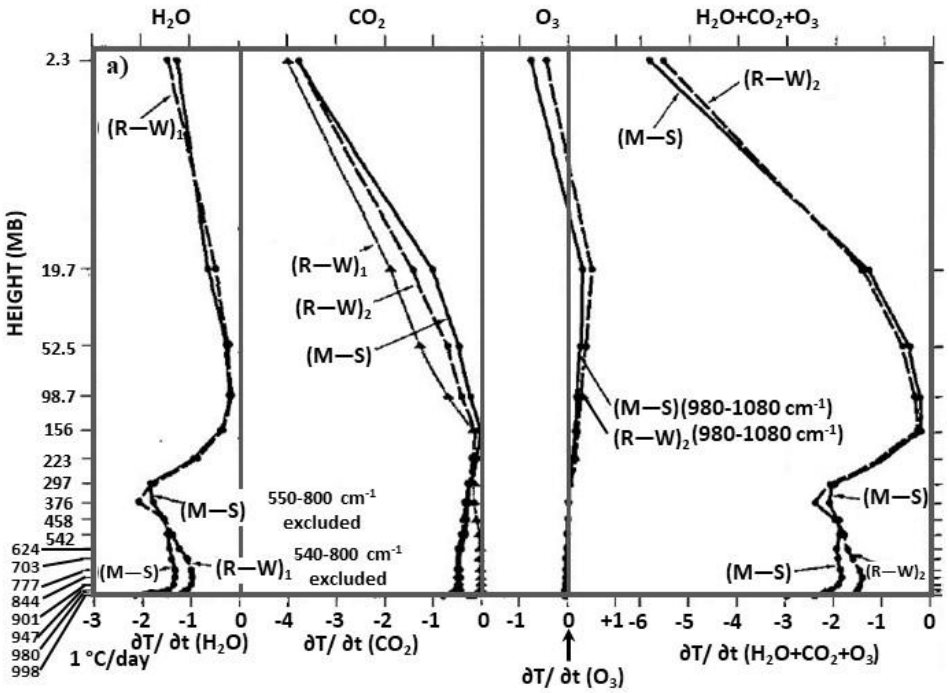

Figure 4: Comparison of heating rated computed by the (M-S) and (R-W) models

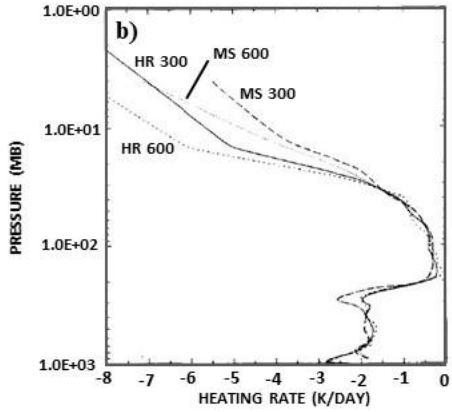

Fig. 3(a) Heating rate profiles computed with HR code for CO_2 concentrations of 300 ppm (solid curve) and 600 ppm (short dash) and profiled computed with MS code for CO_2 concentrations of 300 ppm (long dash) and 600 ppm (dotted) using mid latitude summer profiles.

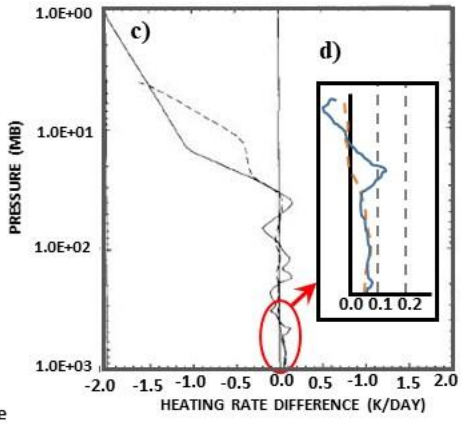

Fig. 3(b) Difference between heating rate profiles for computed CO_2 concentration of 300 ppm and 600 ppm for HR code (solid curve) and MS code (long dash)

Figure 15: a) LWIR cooling rates from Stone and Manabe [1968], b) LWIR cooling rates from Ackerman [1979], c) difference in LWIR cooling rates as the CO_2 concentration is increased from 300 to 600 ppm also from Ackerman [1979], d) lower altitude part of c) on an enlarged scale.

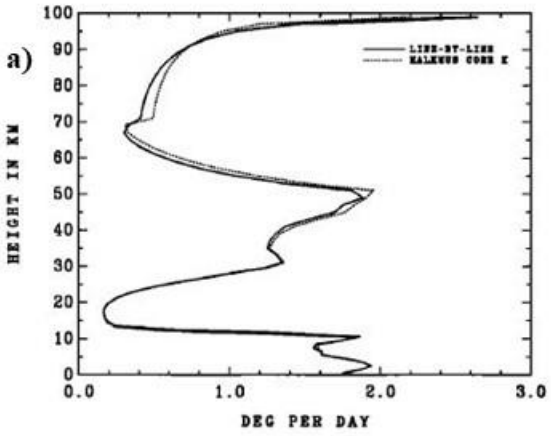

Fig. 16. Radiative cooling rate by atmospheric water vapor. The solid line is the line-by-line cooling rate computed for the McClatchey mid-latitude summer water vapor and temperature profiles using the AFGL 1982 line compilation. The correlated *k* distribution results are shown by the dashed line. Computational details are described in the text.

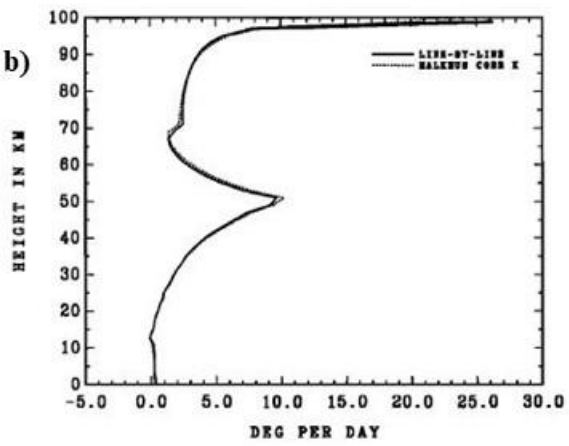

Fig. 17. Radiative cooling rate by CO_2. The solid line refers to line-by-line calculations for a 300-ppmv concentration for the McClatchey mid-latitude summer temperature profile. The dashed curve gives the correlated *k* distribution cooling rate.

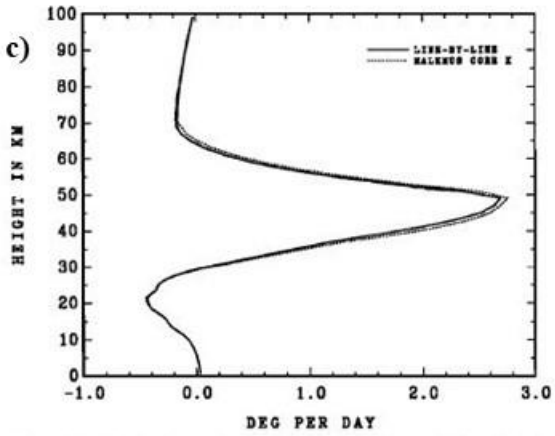

Fig. 20. Radiative cooling rate by ozone. The solid line depicts line-by-line results for the McClatchey mid-latitude summer ozone and temperature distributions. The dashed line gives the correlated *k* distribution results.

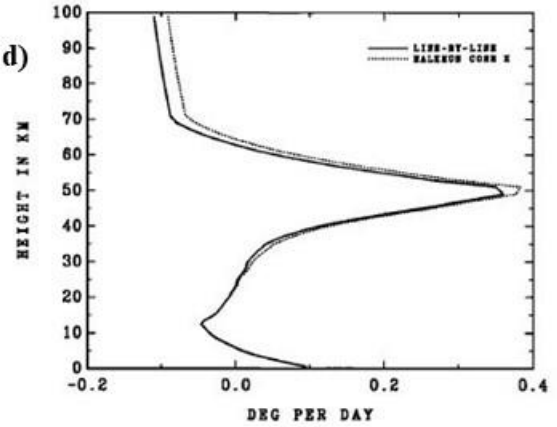

Fig. 22. Radiative cooling rate due to overlapping absorption by CH_4 and N_2O. Explicit line-by-line overlap calculations are shown by the solid line. Correlated *k* distribution treatment of overlapping absorption is given by the dashed line.

Figure 16: LWIR cooling rates from Lacis and Oinas [1991] a) water vapor, b) CO_2, c) ozone and d) CH_4 and N_2O combined.

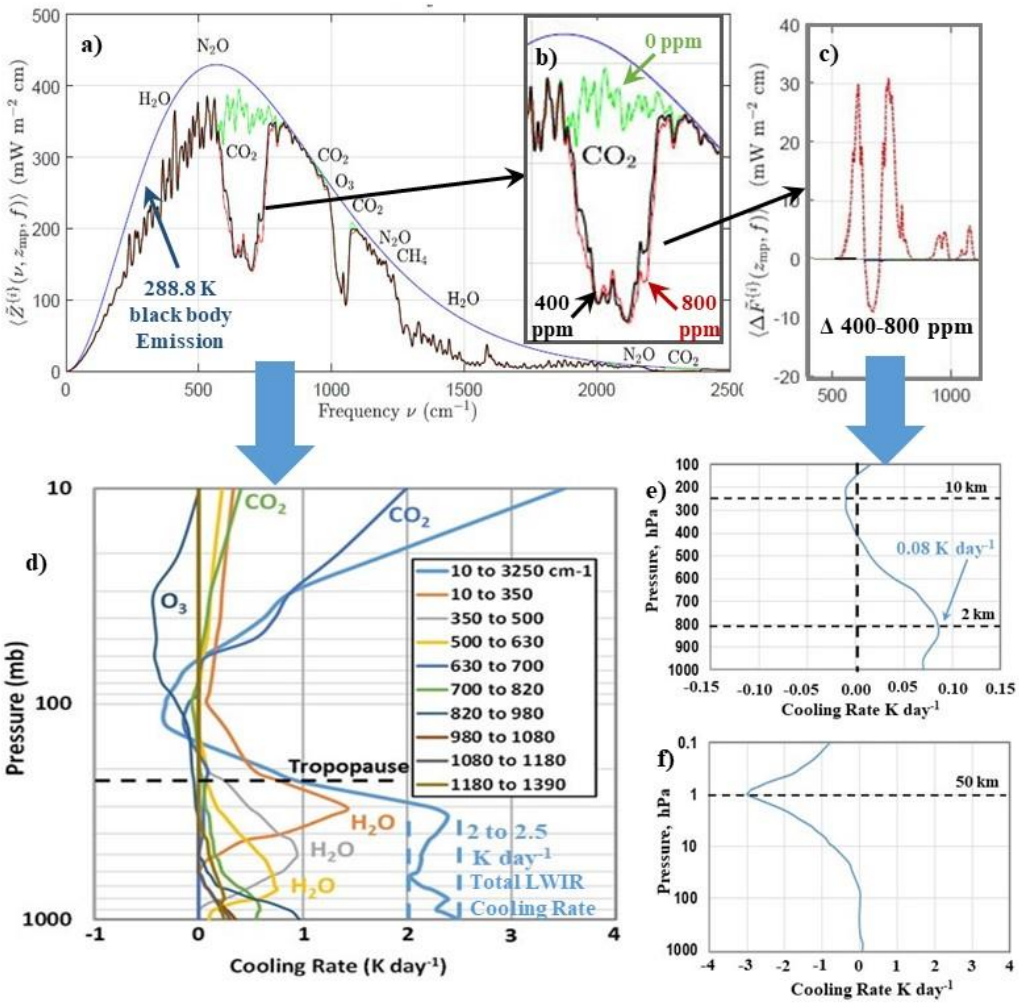

Figure 17: a) The spectrally resolved LWIR emission to space for 0, 400 and 800 ppm CO_2 concentrations, b) the CO_2 emission band on an enlarged scale, c) the difference between the 800 and 400 ppm CO_2 emission, e) the total and band resolved cooling rates vs. altitude for a), e) the changes in the rate of cooling in the troposphere for a CO_2 doubling from 287 to 574 ppm and f) the corresponding changes in the rate of cooling for the stratosphere.

The Dissipation of the Excess Heat in the Troposphere Produced by a CO_2 Doubling

M&W chose to ignore the diurnal and seasonal cycles in the solar flux and the surface temperature and assumed that the small amount of heat released into the troposphere by an increase in the atmospheric concentration of CO_2 could produce a measurable change in surface and tropospheric temperature. Because of molecular line broadening effects, almost all of the downward LWIR flux from the troposphere to the surface is emitted from within the first 2 km layer above the surface and approximately half of this is emitted from within the first 100 m layer (see Figure 13 above). During the day under solar illumination, this layer can be highly turbulent. Figure 18 illustrates the energy transfer processes for an air parcel in the troposphere (within the plane parallel atmosphere approximation). The air parcel is emitting LWIR radiation upwards and downwards at the local temperature. It is also absorbing part of the upward LWIR flux from below and the downward LWIR flux from above. During the day it is also heated directly by the absorption of

the near IR solar flux, mainly by the water vapor overtone bands. The air parcel is also in a turbulent convective flow field. Vertical motion changes the temperature of the air parcel at the local lapse rate. Figure 18b illustrates the dissipation of the absorbed LWIR flux in the troposphere produced by an increase in the atmospheric CO_2 concentration. The small amount of heat that is produced at each level is coupled to the local air parcel and dissipated as wideband LWIR emission, mainly by the water bands. Any change in temperature is too small to measure (CR26).

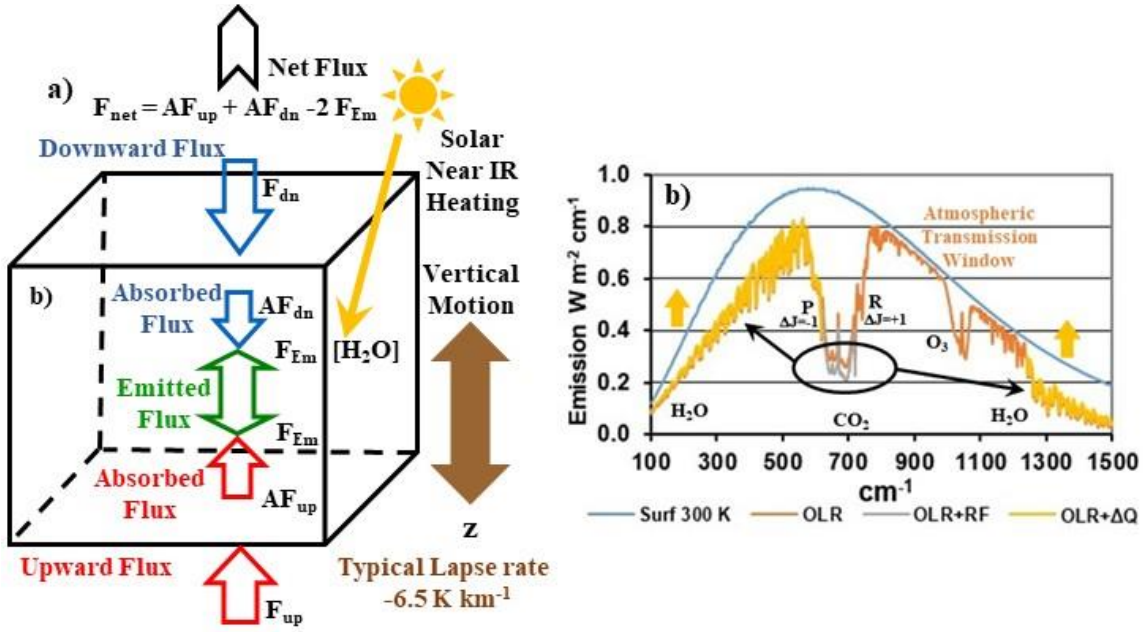

Figure 18: a) The energy transfer processes for a local tropospheric air parcel (in a plane-parallel atmosphere) and b) the dissipation of the absorbed heat from a 'CO_2 doubling' by the normal tropospheric energy transfer processes (schematic). The wavelength specific increase in absorption in the CO_2 P and R bands is dissipated as small changes in broadband LWIR emission and gravitational potential energy.

Figure 19 shows the vertical velocity profile up to 2 km altitude in the turbulent surface boundary layer. This is from Doppler heterodyne LIDAR measurements recorded over 10 hours at the École Polytechnique, south of Paris, July 10th 2005 [Gibert et al, 2007]. The change in vertical velocity is ±2 m s^{-1}. This is sufficient to overwhelm any changes in cooling from a 'CO_2 doubling' as shown in Figure 17e. The LWIR radiative forcings produced by the increase in atmospheric concentration of 'greenhouse gases' cannot change the energy balance of the earth.

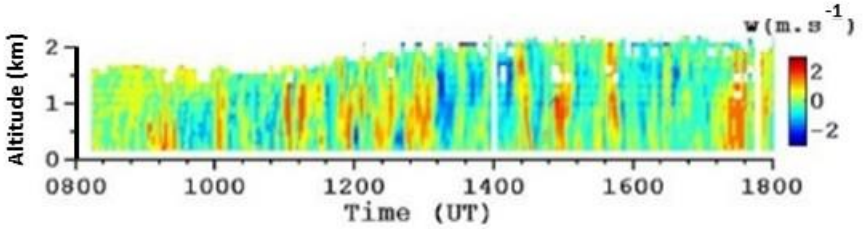

Figure 19: Vertical velocity profile in the turbulent boundary layer recorded over 10 hours at the École Polytechnique, south of Paris, July 10th 2005 using Doppler heterodyne LIDAR.

Manabe's group at NOAA, Hansen's group at NASA and all of the climate modelers that copied them failed to perform any serious validation of the models that they were using. The number series of the average temperature profile generated by their models agreed with the number series obtained by averaging the measured data. This was deemed sufficient. The underlying assumptions were never questioned. Detailed measurements of the energy transfer processes at the land-air interface were available from the Great Plains Turbulence Field Program conducted from August 1 to September 8, 1953 at O'Neill, Nebraska [Letteau and Davidson 1957a, 1957b]. Figure 20 shows the measurement of the vertical velocity from the second observational period, August 13. These measurements were obtained by filming the drift of smoke puffs generated by dropping a magazine of smoke cartridges from a helicopter. When these measurements are combined with the radiosonde temperature profiles (see Figure 30 below), the turbulent temperature changes can be estimated. This invalidates the MW67 model. The small change in the daily rate of LWIR cooling produced by a 'CO_2 doubling' cannot accumulate in the troposphere.

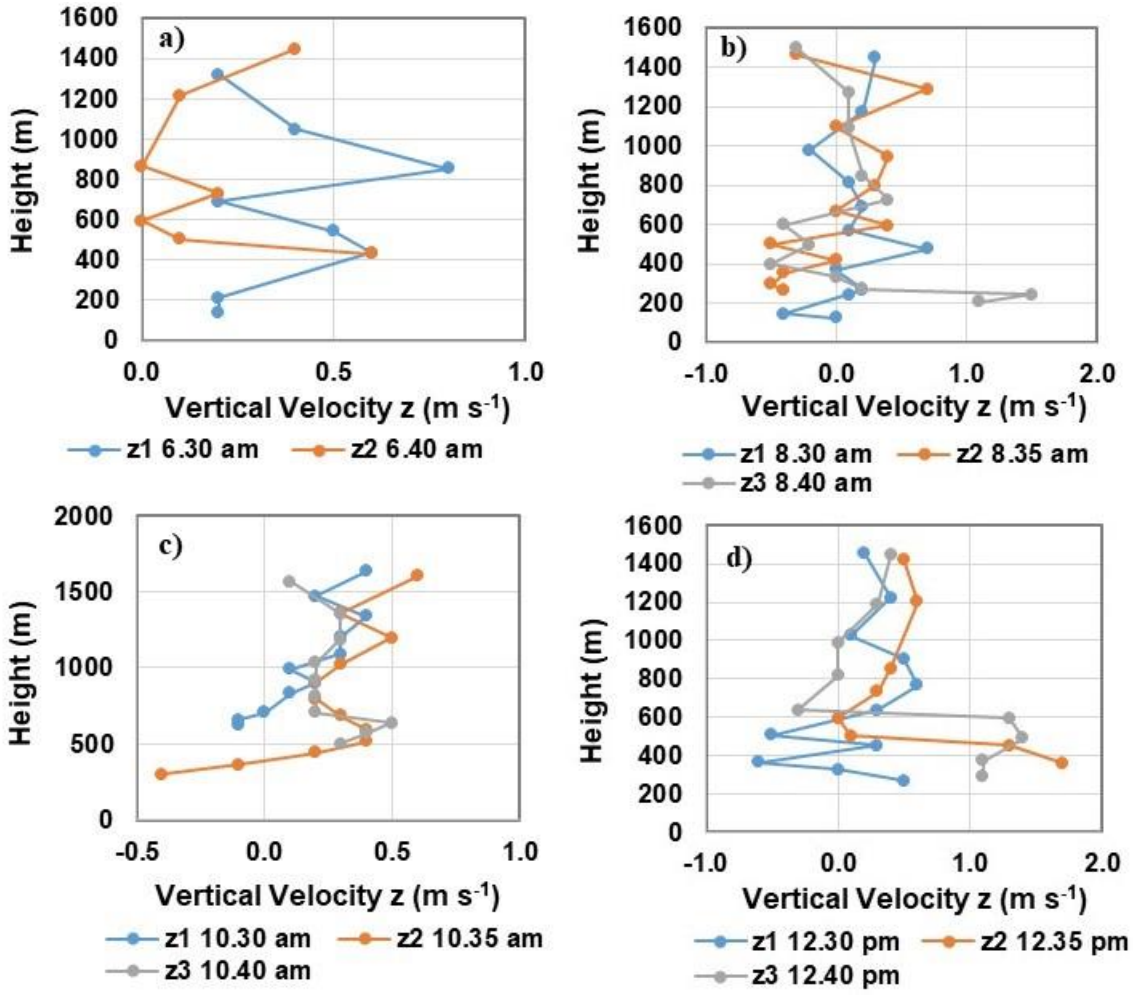

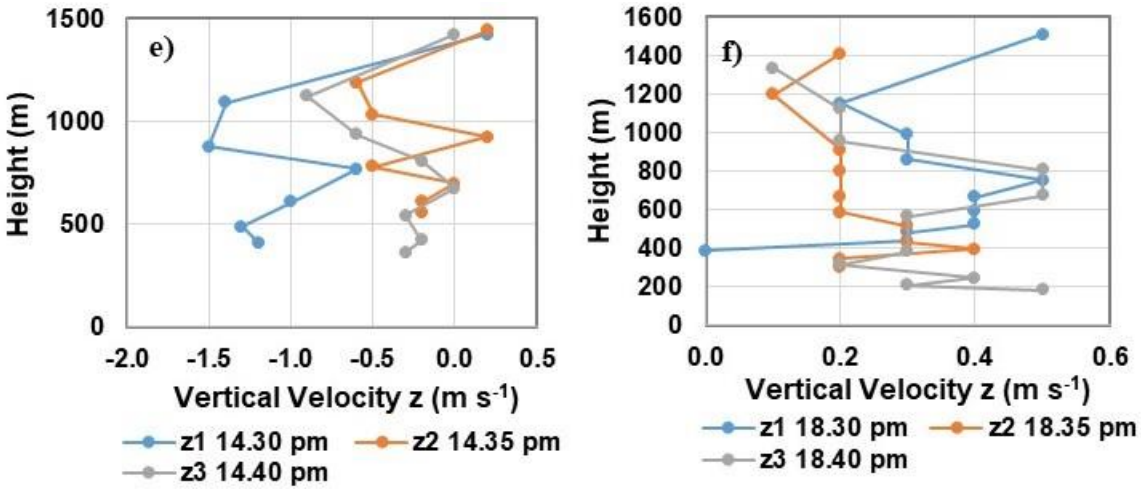

Figure 20: Vertical velocity profiles measured at O'Neill, Nebraska on August 13, 1953.

The Coupling of the LWIR Flux to the Ocean Surface

MW67 only considered atmospheric energy transfer. The 'ground' used in the MW67 model was a partially reflective blackbody surface with zero heat capacity. It was just a lower mathematical boundary to the radiative transfer model. The surface temperature was adjusted so that the LWIR flux emitted at the top of the model atmosphere (TOMA) matched the absorbed solar flux. Any energy imbalance at the surface was attributed to surface cooling by convection. This is illustrated in Figure 21 from MS64, Table 3. When the real energy transfer properties of the surface are considered, a very different picture emerges.

Table 3: Integrated heat balance components of thermal equilibrium (Ly min^{-1}) of the atmospheres with and without clouds shown in Fig. 8a. Hemispheric annual mean components obtained by London are also shown for comparison.

	Ly min^{-1}			W m^{-2}		
	Thermal Equilibrium		Heat Balance	Thermal Equilibrium		Heat Balance
	Clear sky	Average Cloudiness	London	Clear sky	Average Cloudiness	London
Net outgoing LWIR at TOA	0.4287	0.3266	0.324	300	229	227
Net incoming SW radiation at TOA	0.4286	0.3266	0.324	300	229	227
LW atmospheric heating	-0.2802	-0.2412	-0.234	-196	-169	-164
SW atmospehric heating	0.0927	0.0901	0.087	65	63	61
LW surface Heating	-0.1485	-0.0854	-0.09	-104	-60	-63
SW surface heating	0.336	0.2365	0.237	235	166	166
Eddy transport (surface convective cooling)	0.1875	0.1555	0.147	131	109	103

Figure 21: 1-D RC climate model energy balance for fixed absolute humidity from Table 3, MS64. The average flux values are also shown in modern units, W m^{-2}.

Over the oceans, the surface is almost transparent to the solar flux. The diurnal temperature rise is small and the bulk ocean temperature increases until the water vapor pressure at the surface is sufficient for the excess absorbed solar heat to be removed by wind driven evaporation. The

sensible heat flux is usually small, less than 10 W m^{-2}. The penetration depth of the LWIR flux into the ocean surface is less than 100 micron. This is illustrated in Figure 22 [Hale and Querry, 1973]. The net LWIR flux, the wind driven evaporation or latent heat flux and the sensible heat flux are coupled together at the surface and should not be analyzed separately. The cooler water produced at the surface sinks and is replaced by warmer water from the bulk ocean below. This allows the evaporation to continue at night. Figure 23 shows the long term zonal average sensitivity of the latent heat flux to the wind speed. This is calculated from the long term zonal average ocean latent heat flux and wind speed data given by Yu et al [2008]. Over the ±30° latitude bands, the sensitivity is at least 15 W m^{-2}/m s^{-1}. The increase in downward LWIR flux to the surface produced by the observed 140 ppm increase in atmospheric CO_2 concentration is approximately 2 W m^{-2} [Harde, 2017]. Within the ±30° latitude bands, this is dissipated by an increase in wind speed near 13 cm s^{-1}. For comparison, the long term 1σ variation in wind speed along the equator, measured by the TRITON buoy network is near 2 m s^{-1} (CR23). The average annual increase in atmospheric CO_2 concentration at present is near 2.4 ppm. This corresponds to an annual increase of 0.034 W m^{-2} in the downward LWIR flux to the surface which is dissipated by an increase in wind speed near 2 millimeters per second. Any change in ocean temperature produced by the current annual increase in the atmospheric CO_2 concentration is therefore too small to measure.

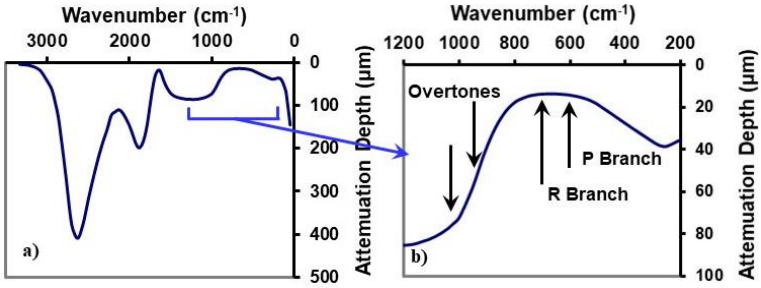

Figure 22: The penetration depth (99% absorption) of the LWIR flux into water a) below 3300 cm^{-1} and b) 1200 to 200 cm^{-1}. The locations of the main CO_2 absorption bands and the overtones are indicated.

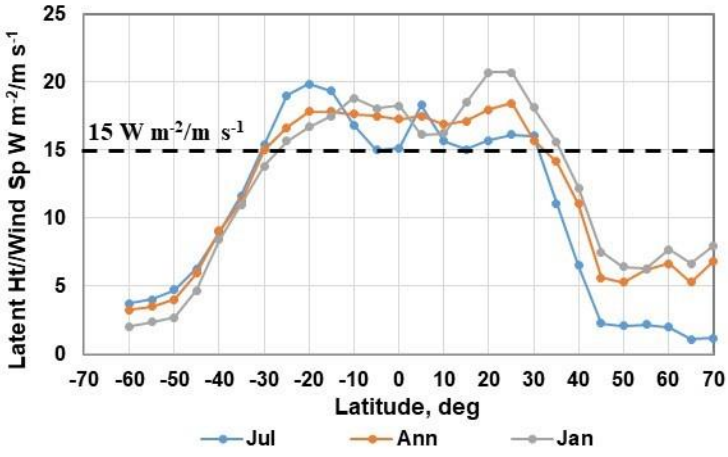

Figure 23: The sensitivity of the ocean latent heat flux to the wind speed.

Figure 24 shows the hourly flux terms, surface and air temperatures, and related data recorded by the TRITON buoy moored on the equator at 165° E for 14 days starting March 1 2008 [TRITON, 2021]. Figure 24a shows the solar flux and Figure 24b the surface and air temperatures. Figure 24c shows the latent heat flux, LH, the net IR flux, the sensible heat flux, SH and the total LH + net IR + SH flux. Figure 24d shows the net flux, 24e the wind speed and 24f the relative humidity. The maximum, minimum and average values and the 1σ standard deviations for the data presented in Figure 24 are summarized in Table 1. There is no requirement for an exact flux balance between the absorbed solar flux and the surface cooling flux. Over the 14 day period shown here there was an average net heating flux into the ocean of 124 W m^{-2}. Any small increase in the downward LWIR flux to the surface produced by an increase in greenhouse gas concentration is coupled to the total cooling flux at the surface and cannot have any effect on the bulk ocean temperature below. The cooling flux interacts with a surface layer that is approximately 100 micron (0.004 inches) thick. Over an area of 1 square meter the initial interaction volume is 100 cm^3.

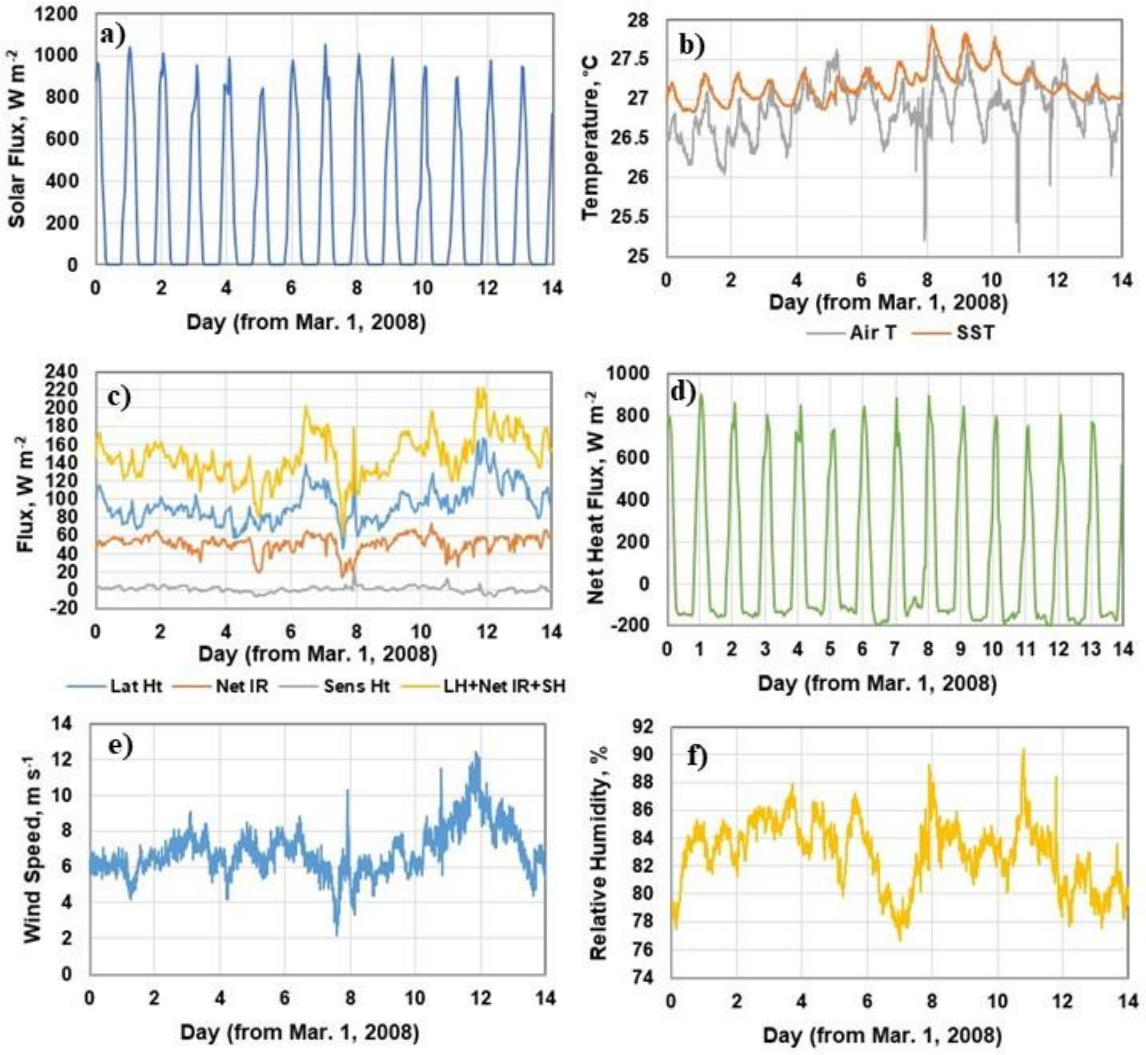

Figure 24: Hourly flux terms, surface and air temperatures, wind speed and relative humidity recorded from March 1 to March 14, 2008 by the TRITON buoy moored at the equator at a latitude of 165° E.

	SW	Air T	SST	Lat Ht	Net IR	Sens Ht	LH+NetIR+SH	Net Heat	Wsp	RH
Max	1055	27.1	27.3	167	75	20	222	902	7.6	85.7
Min	0	26.1	26.8	46	15	-7	62	-222	4.2	77.5
Av	272	26.5	27.0	94	52	1	148	124	6.1	83.1
Stdev	350	0.23	0.15	20	10	3	25	351	0.59	1.80

Table 1: Maximum, minimum and average values and 1σ standard deviations for the data presented in Figure 24.

Based on the discussion in this section, any small increase in downward LWIR flux from the lower troposphere to the surface produced by an increase in atmospheric greenhouse gas concentration cannot produce a measurable change in ocean surface temperature. The largest cooling term is the latent heat flux. This depends on the humidity gradient and the wind speed. The energy transfer processes that determine the ocean surface temperature are considered in more detail in CR23.

The Coupling of the LWIR Flux to the Land Surface

Over land, all of the flux terms are absorbed by a thin surface layer. The surface temperature initially increases after sunrise as the solar flux is absorbed. This establishes a thermal gradient with both the cooler air above and the subsurface ground layers below. The surface-air gradient drives the evapotranspiration and the subsurface gradient conducts heat below the surface during the first part of the day after sunrise. Later in the day, as the surface cools, the subsurface gradient reverses and the stored heat is returned to the surface. As the land and air temperatures equalize in the evening, the convection stops and the surface cools more slowly by net LWIR emission until after sunrise the following day. This convection transition temperature is reset each day by the local weather system passing through. Almost all of the absorbed solar heat is dissipated within the same diurnal cycle. The heat transfer is localized. The diurnal temperature change is limited to a shallow depth, typically 0.5 to 2 m, and the seasonal temperature variations may extend to 5 m below the surface (CR23) [Clark, 2013]. There are also characteristic phase shifts or time delays between the peak solar flux and the temperature response that are clear evidence of a non-equilibrium thermal response. These are not a new discovery. The subsurface seasonal phase shift was described by Fourier in 1824 [Fourier, 1824]. The soil temperatures at depths from 0.5 to 80 cm and the 2 m air temperature recorded at a monitoring site at O'Neill, Neb., August 13, 1953, are shown in Figure 25 [Lettau and Davidson 1957b]. The surface temperature phase shift, δt, is indicated. Below the surface, the temperature rise decreases and the phase shift increases with the depth. At the surface, the temperature rise is 22 °C. The surface air temperature rise at 1.5 m above the surface is 15 °C. There is almost no measurable diurnal phase shift below 50 cm depth. See CR23 for further discussion.

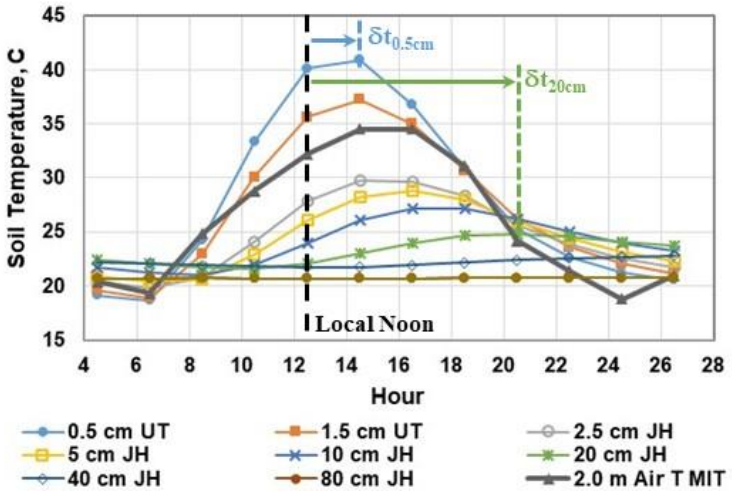

Figure 25: 2 m air temperature and subsurface temperatures measured at O'Neill, Neb., August 13, 1953. The temperature rise decreases and the time delay or phase shift relative to the peak solar flux increases with depth.

The various flux terms interact with the surface and change the temperature at the land-air interface. However, the weather station temperature is the meteorological surface air temperature (MSAT) measured in a ventilated enclosure located at eye level, 1.5 to 2 m above the ground [Oke, 2006]. In general, the minimum MSAT and the minimum surface temperature are similar, but the maximum surface temperature is larger than the maximum MSAT (CR23). The minimum and maximum temperatures are determined by different energy transfer processes. The minimum temperature is reset each day by the bulk surface air temperature of the local weather system passing through. The maximum surface temperature is set by the balance between the solar heating, the combined net LWIR flux and evapotranspiration (moist convection) and the subsurface thermal transport. The maximum MSAT is determined by the mixing of the warm air rising from the surface with the cooler air at the level of the MSAT thermometer. The important physical variables in the weather station temperature data are therefore the minimum MSAT and the ΔT or difference between the maximum and minimum MSAT. The average MSAT, $(T_{max} + T_{min})/2$, has little useful meaning.

To illustrate the normal variation in the MSAT record, the 1981 to 2010 30 year daily climate averages for the O'Neill, Neb. weather station #256290 are shown in Figure 26 [WRCC, 2022]. The 1σ standard deviations and the ΔT (T_{max} - T_{min}) values are also shown. There is a phase shift of approximately 30 days between the peak solar flux at summer solstice, day 172 and the peak seasonal temperature response. In addition, the ΔT values remain within the approximate range 13.4 ±2 °C for the entire year while the temperature variation is ±10 °C. The 1σ temperature standard deviations increase from approximately 4 °C in summer to 8 °C in winter.

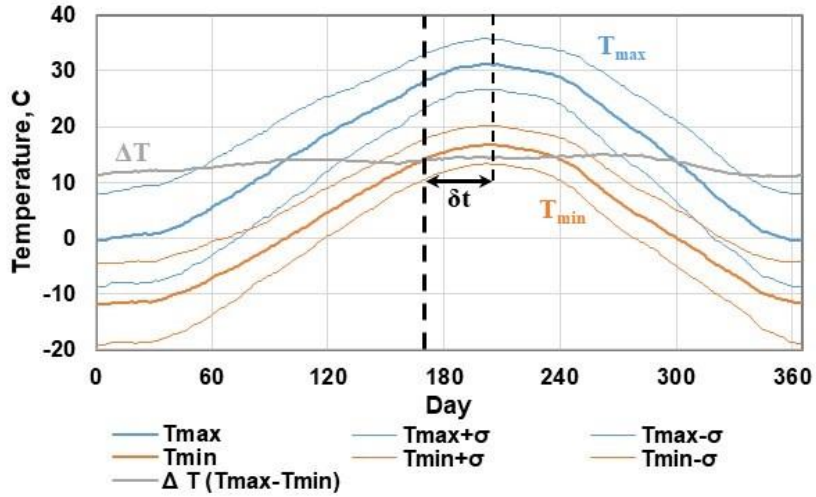

Figure 26: 1981-2010 daily climate averages for O'Neill, Neb., Station #256290. The 1 σ standard deviations and the ΔT (T_{max} -T_{min}) are also shown. The seasonal phase shift, δt is indicated.

There are three features in Figure 26 that require further consideration. First, the 1σ standard deviations are quite large. Second, the variation in ΔT is smaller than the changes in the max and min temperatures. Third, the seasonal phase shift is not produced locally.

The 1 σ standard deviation range in the daily average temperatures is from ±3.4 to ±8.7 °C. The larger values occur at the beginning and end of the year when the temperatures are lower. As discussed in more detail CR23, convective cooling of the surface occurs during the day when the solar heated surface is warmer than the air temperature. Each evening there is a convective transition temperature at which the surface and surface air temperatures approximately equalize and the dominant cooling term becomes the net LWIR flux emitted into the LWIR transmission window. This transition temperature is reset each day by the local weather system passing through. The variation in transition temperature is similar to the variation in the minimum temperatures. The measured maximum and minimum temperatures and ΔT values from the 1953 O'Neill observation site weather station data are plotted in Figure 27a with the climate data from Figure 26. The differences from the climate means are plotted in Figure 27b. The maximum difference is +8.8 °C for Sept 8. Second, the smaller variation in ΔT compared to the min and max temperatures shows that there is a control mechanism that regulates the daily temperature increase. The moist convection (evapotranspiration) or sensible and latent heat fluxes increase with the solar flux and the rate of surface cooling increases. The latent heat flux also depends on the available surface moisture. This is discussed in more detail in CR23. Third, the source of the phase shift is the convective transition temperature related to the weather systems passing through. Many of these weather systems are formed over the ocean and the bulk air temperature is influenced by the ocean temperature along the path of the weather system. The source of the seasonal phase shift is the ocean response to the solar flux. There are also longer term temperature fluctuations related to the ocean oscillations.

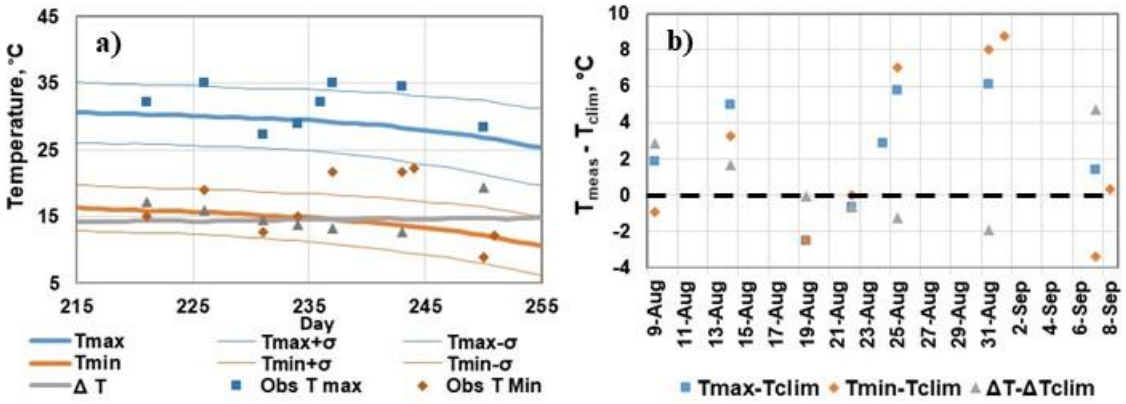

Figure 27: The maximum and minimum air temperatures and ΔT values from the O'Neill Test Site weather station data, plotted with the 1981-2010 30 year climate average data for O'Neill, Nebraska and b) deviations of the measured temperatures and delta temperatures from the climate averages shown in a).

This analysis demonstrates that the day to day variation in surface temperatures is much larger than any change that can be produced by a doubling of the CO_2 concentration. The period of record for the O'Neill weather station extends back at least to 1920, so the 1920 to 1950 climate data would have been available to M&W for model validation.

The Fixed Relative Humidity Assumption and 'Water Vapor Feedback'

The fixed relative humidity (RH) distribution used in MW67 is based on average hemispherical planetary values as shown in Figure 28a (MW76, figure 3). Most of the model calculations were performed using this linear RH distribution with a surface RH (h_*) of 77%. The vertical distributions of radiative equilibrium temperature when the surface RH is changed to 20, 50 and 100% are shown in Figure 28b (MW67, figure 11). The average relative humidity distribution used in MW67 is a mathematical construct that gives a reasonable match to average data for the atmospheric temperature profile. M&W made no attempt to validate their model using any thermal engineering analysis of the surface energy transfer. They did not understand that the diurnal and seasonal changes in temperature and humidity were sufficiently large that the changes in average LWIR flux and temperature in their model produced by changes in the CO_2 concentration were too small to measure.

As shown above in Figure 13c, almost all of the downward LWIR flux to the surface is emitted within the first 2 km layer of the troposphere and approximately half of this comes from within the first 100 m layer. An altitude of 2 km corresponds to an atmospheric pressure near 800 mb. Near the surface, both the relative and absolute humidity can change during the diurnal cycle. Figure 29 shows the humidity changes recorded at the O'Neill, Nebraska test site during the second observational period, August 13 to 14, 1953 related to the temperature changes shown in Figure 25 above. The RH decreased from approximately 65% at 6:30 am to 35% at 4:30 pm and then increased to approximately 70% by 2:30 am the following morning. The absolute humidity increased from about 14 mb at 2:30 am to 20 mb at 12:30 pm and decreased back near 15 mb by 00:30 am the following morning. Figure 30 shows the radiosonde data, temperature (°C) and

relative humidity (%) vs pressure (mb) recorded at O'Neill during the second observation period. The calculated water vapor concentration (mb) derived from the temperature and RH data is also plotted. These data illustrate the variability in temperature and humidity during the day. The RH range is between 20 and 80%. Any small increase in temperature produced by an increase in downward LWIR flux to the surface from an increase in CO_2 concentration will be too small to measure in the normal variation of the diurnal and seasonal temperature and humidity.

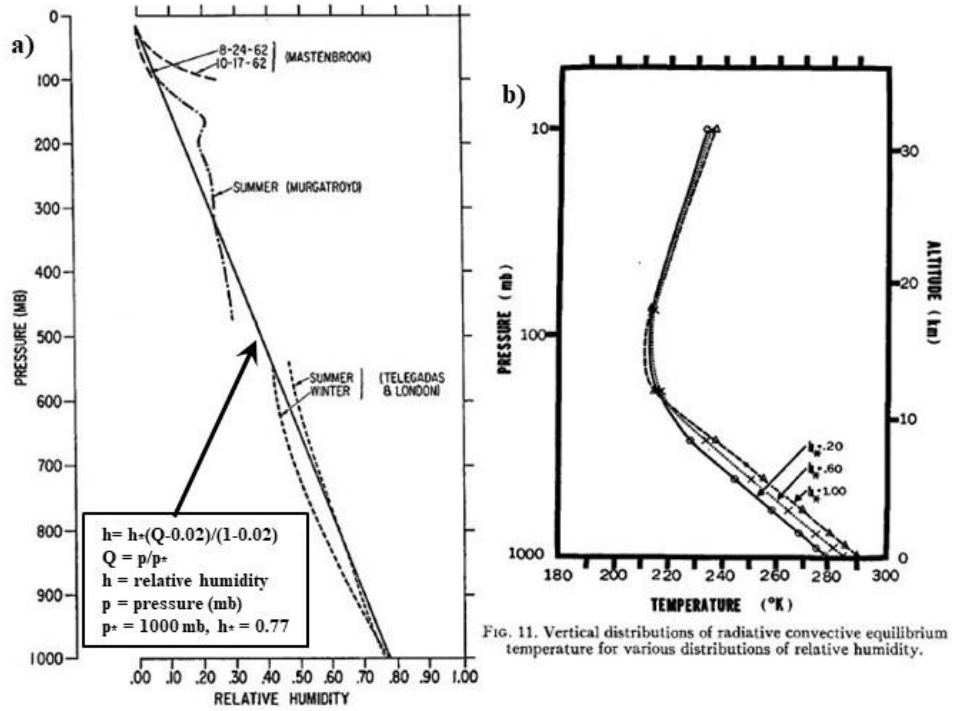

FIG. 3. Vertical distribution of relative humidity (Mastenbrook, 1963; Murgatroyd, 1960; Telegadas and London, 1954).

FIG. 11. Vertical distributions of radiative convective equilibrium temperature for various distributions of relative humidity.

Figure 28: a) The humidity distribution used in MW67 and b) changes in the surface temperature and atmospheric temperature profile produced by changing the surface humidity h_* in the MW67 model.

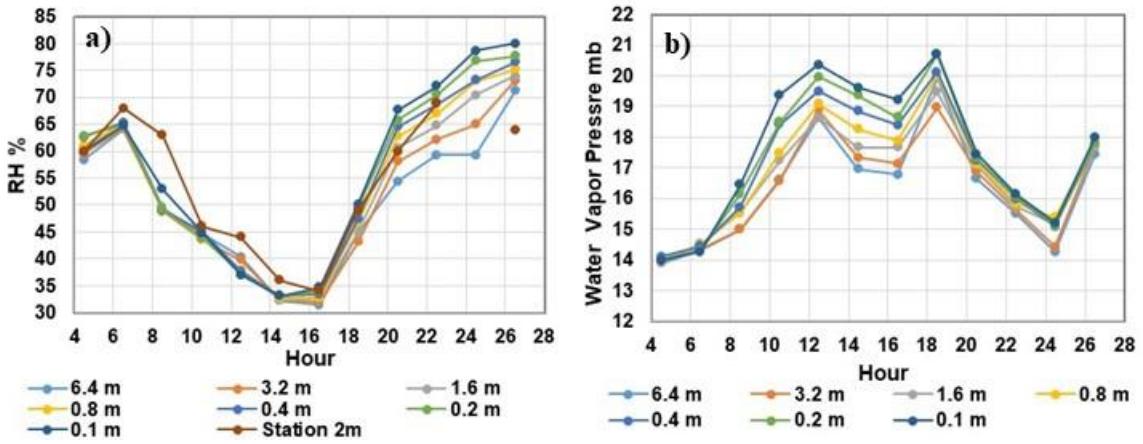

Figure 29: a) relative humidity, % and b) absolute humidity, mb recorded at O'Neill, Nebraska, August 14 - 14, 1953.

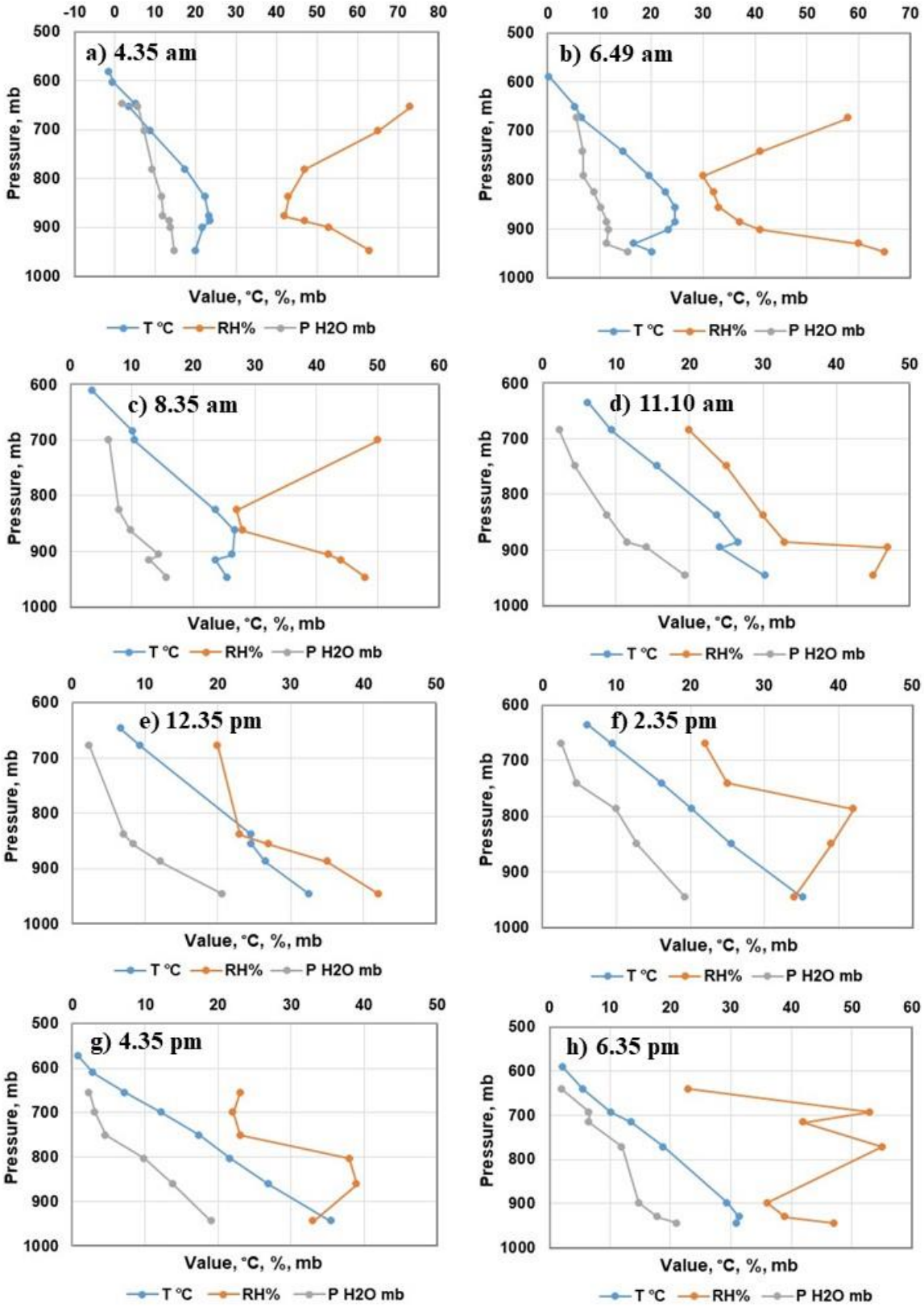
a) 4.35 am
b) 6.49 am
c) 8.35 am
d) 11.10 am
e) 12.35 pm
f) 2.35 pm
g) 4.35 pm
h) 6.35 pm
Pressure, mb
Value, °C, %, mb
T °C
RH%
P H2O mb

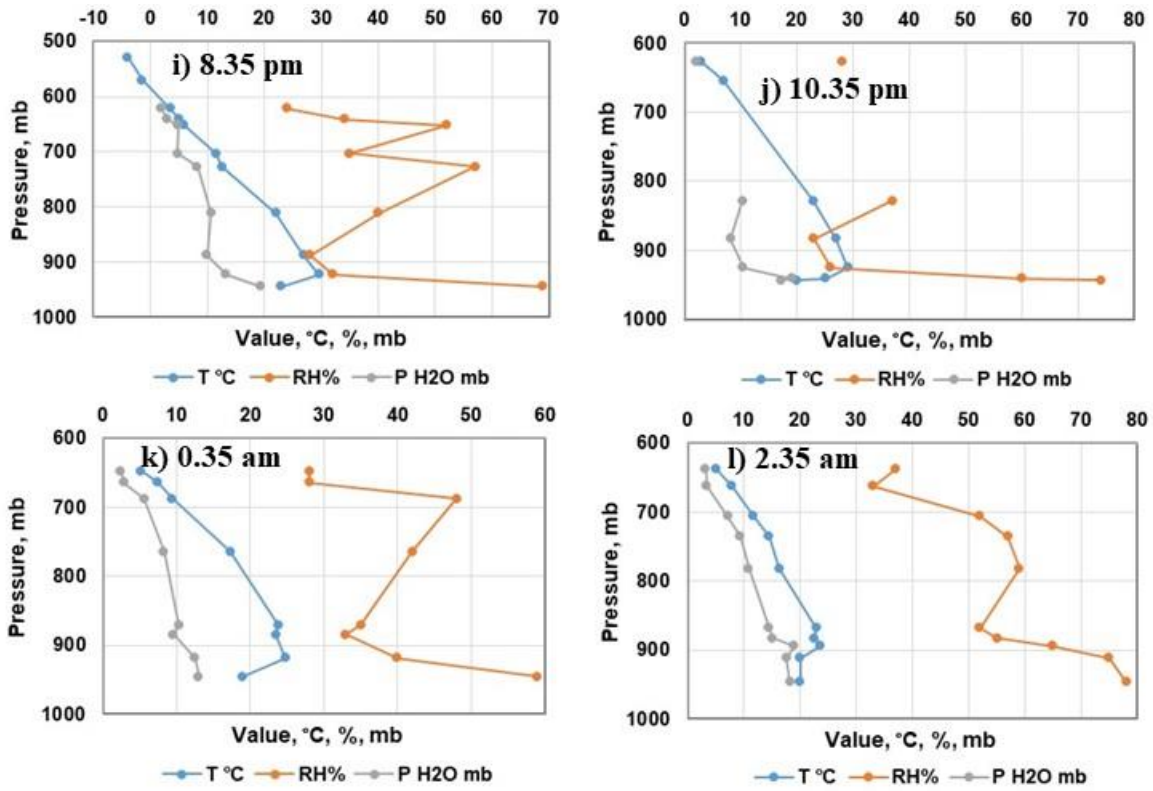

Figure 30: Radiosonde data, temperature (°C) and relative humidity (%) vs pressure (mb) recorded during the second observation period. The calculated water vapor concentration (mb) is also shown.

The surface in MW67 was a partially reflective blackbody surface with zero heat capacity. It was simply the lower boundary to the radiative transfer calculation. As the surface temperature increased, the imposed relative humidity profile created an increase in the absolute water vapor concentration. This led to an increase in the downward LWIR flux from water vapor that in turn created a feedback by increasing the surface temperature and amplifying the CO_2 warming. This is simply an artifact of the steady state model. When the time dependent surface energy transfer is introduced, a different picture emerges.

This may be illustrated by considering the Grasslands data set described in CR23. This is a year of temperature and flux data recorded at an advanced AmeriFlux monitoring site located in Limestone Canyon Regional Park, near Irvine, S. California in 2008. The complete data set consisted of half hour averages of 17 parameters: friction velocity, air temperature, wind direction, wind speed, CO_2 flux, H_2O flux, sensible heat flux, latent heat flux, CO_2 concentration, H_2O concentration, incoming photosynthetic active radiation, reflected photosynthetic active radiation, incoming global solar radiation, reflected global solar radiation, relative humidity, precipitation and net radiation. The maximum and minimum daily air temperatures and the 8 day satellite average min/max skin (surface) temperatures for the year are shown in Figure 31. The various temperature spikes through the year are caused by the transition from coastal onshore winds to desert offshore winds with a decrease in humidity and an increase in air temperatures from downslope wind effects. The heating is caused by air compression as the dry air descends ~1 km

from the desert to the coast. The minimum surface and air temperatures are similar, but the maximum surface temperature is higher than the maximum air temperature. The surface temperature also increases with the air temperature, although the surface temperatures are 8 day averages that do not change as fast as the air temperatures.

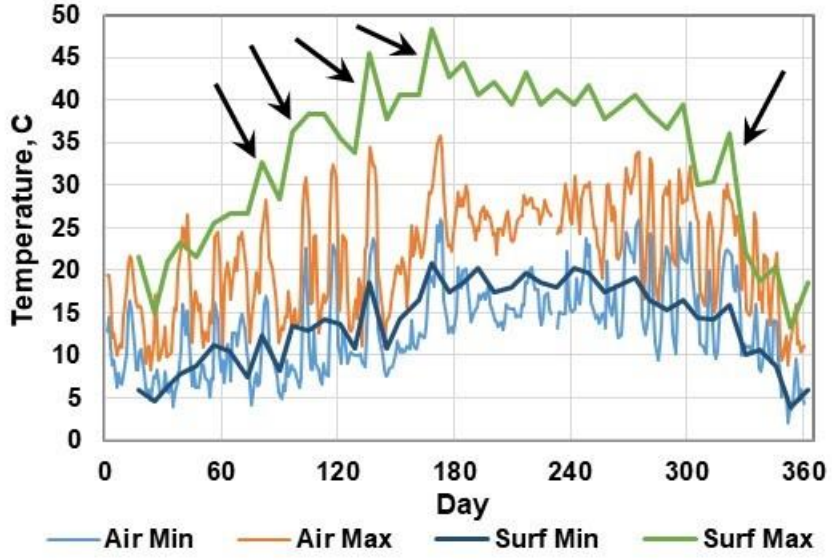

Figure 31: Daily maximum and minimum air temperatures and 8 day average surface temperatures for 2008 Grasslands data set. Some of the temperature spikes caused by downslope wind effects are indicated by the arrows.

Figure 32a shows the full air temperature data set and Figure 32b shows the relative humidity. This varies from less than 10% to over 90%. The upper limit is set by the instrument. The temperature spikes from the offshore flow indicated in Figure 31 are also shown in Figures 32a and 32b. Inspection shows that they correspond to periods of low humidity. Although such numbers have little physical meaning, the annual average temperature is 17.2 ± 6.5 °C and the annual average humidity is 55 ± 27.5 %.

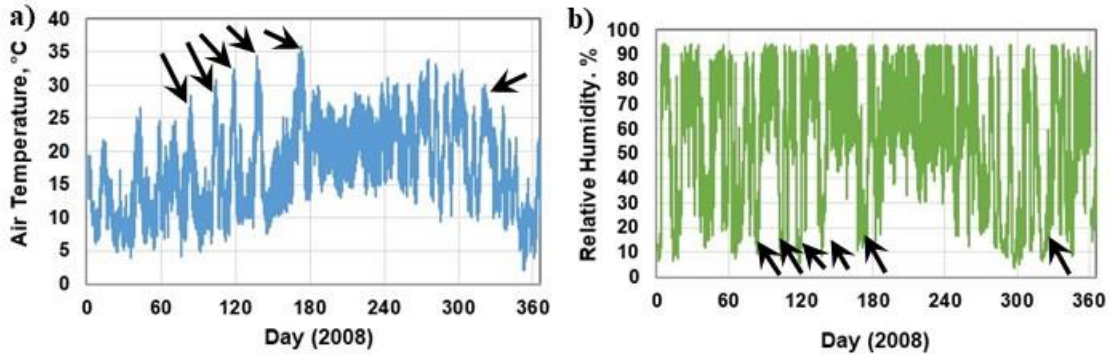

Figure 32: a) The full Grasslands 2008 half hour air temperature and b) the relative humidity record

Changes in humidity and cloud cover alter the net LWIR cooling flux emitted by the surface into the LWIR atmospheric transmission window. The magnitude of the net LWIR flux increases with

decreasing humidity and decreases with increasing humidity and cloud cover. The average daily night time net LWIR fluxes for 2008 are shown in Figure 33. The high values for the net LWIR flux are characteristic of offshore flow conditions associated with strong downslope winds known as Santa Ana winds. The low values indicate cloud cover or a marine layer over the measurement site. The annual average is 44 ±16 W m^{-2} (1σ standard deviation).

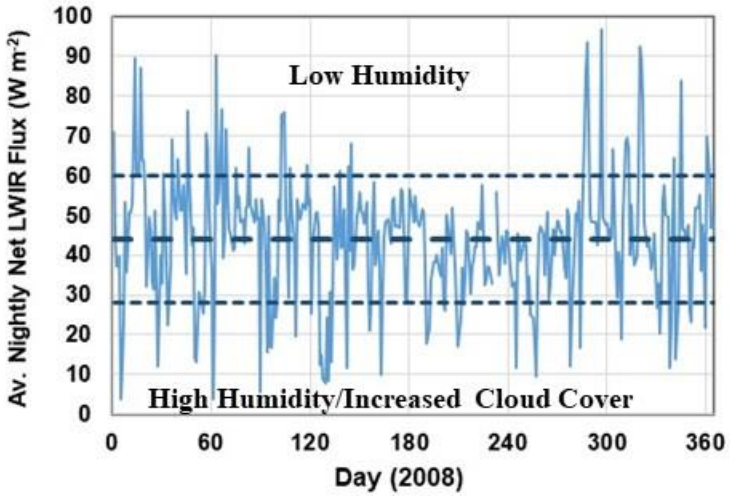

Figure 33: The average daily nighttime net LWIR flux recorded at the Grasslands Site.

Most rainfall in S. California occurs during the winter months. The vegetation then dries out over the summer leading to increased fire risk during offshore flow conditions. The cumulative daily latent heat fluxes for daytime and nighttime conditions are shown in Figure 34a. The ratio of the latent heat flux to the solar flux is shown in Figure 34b. Almost all of the evaporation occurs during the day. The peak latent heat flux occurs in March as the soil and vegetation dry out after the winter rains. The maximum value of the latent heat flux is 6 MJ m^{-2} day^{-1} and the maximum fraction of the solar flux converted to latent heat is near 0.4.

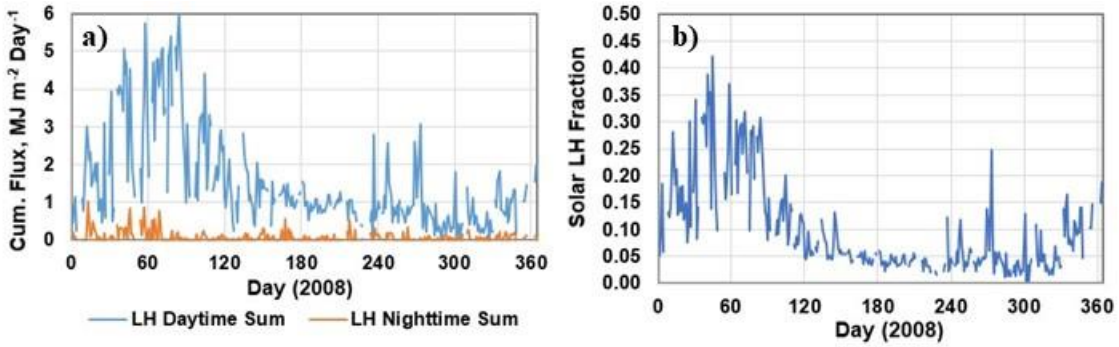

Figure 34: a) Cumulative daily latent heat flux for daytime and nighttime conditions and b) ratio of the daytime latent heat flux to the solar flux.

A doubling of the atmospheric CO_2 concentration from 280 to 560 ppm produces a decrease in LWIR flux at TOA of approximately 3.7 W m^{-2} [IPCC, 2013] and a similar increase in flux from the lower troposphere to the surface. Since 1800, the atmospheric concentration of CO_2 has

increased by approximately 140 ppm from 280 to 420 ppm. This has produced a decrease in flux at TOA of about 2 W m^{-2} with a similar increase in the downward LWIR flux to the surface. The increase in CO2 concentration is shown in figure 35a [Keeling, 2023]. The changes in upward LWIR flux at TOA and the downward LWIR flux to the surface are illustrated in Figure 35b [Harde, 2017]. At present, the increase in average atmospheric CO_2 concentration is near 2.4 ppm per year and the corresponding increase in downward flux to the surface is approximately 0.034 W m^{-2} per year. There is also a seasonal fluctuation near 8 ppm per year.

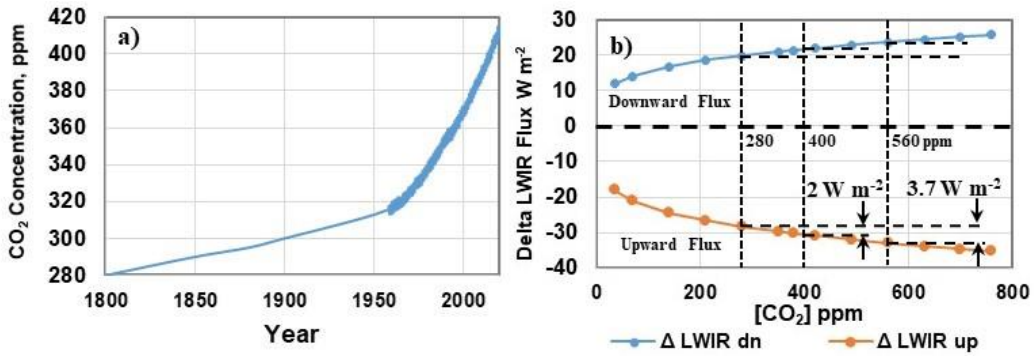

Figure 35: a) The increase in atmospheric CO_2 concentration from 1800 (Keeling curve) and b) Calculated changes in atmospheric LWIR flux produced by an increase in atmospheric CO_2 concentration from 0 to 760 ppm.

In MW67, a doubling of the atmospheric CO_2 concentration from 300 to 600 ppm produced an increase in equilibrium surface temperature for clear sky of 2.9 °C. There are two errors in this calculation. First, the initial increase in surface temperature is a mathematical artifact of the steady state calculation. Second, there is no 'water vapor feedback'. How can an annual increase in downward LWIR flux of 0.034 W m^{-2} have any effect on the temperatures shown in Figures 31 and 32a? How can this small change in flux be detected in the variation of the downward LWIR flux shown in Figure 33? The latent heat flux is a cooling flux. There is no equilibrium. As shown in Figure 34, the latent heat flux reaches a peak near 6 MJ m^{-2} per day (70 W m^{-2}) near the spring equinox and decreases to much lower values in the fall as the ground and the vegetation dry out. The water vapor molecules that carry the latent heat flux are removed from the surface air layer by convection.

The Time Marching or Integration Error

The time integration error in MW67 is illustrated in Figure 36 (adapted from MW67 Figure 2). When the CO_2 concentration is doubled, the maximum change in the tropospheric cooling rate is +0.08 K (Ackerman, 1979, Iacono et al, 2008. As discussed above in connection with Figures 17 through 20, this small change in tropospheric temperature is too small to measure and cannot accumulate over time. In addition, there can be no temperature amplification from a 'water vapor feedback'.

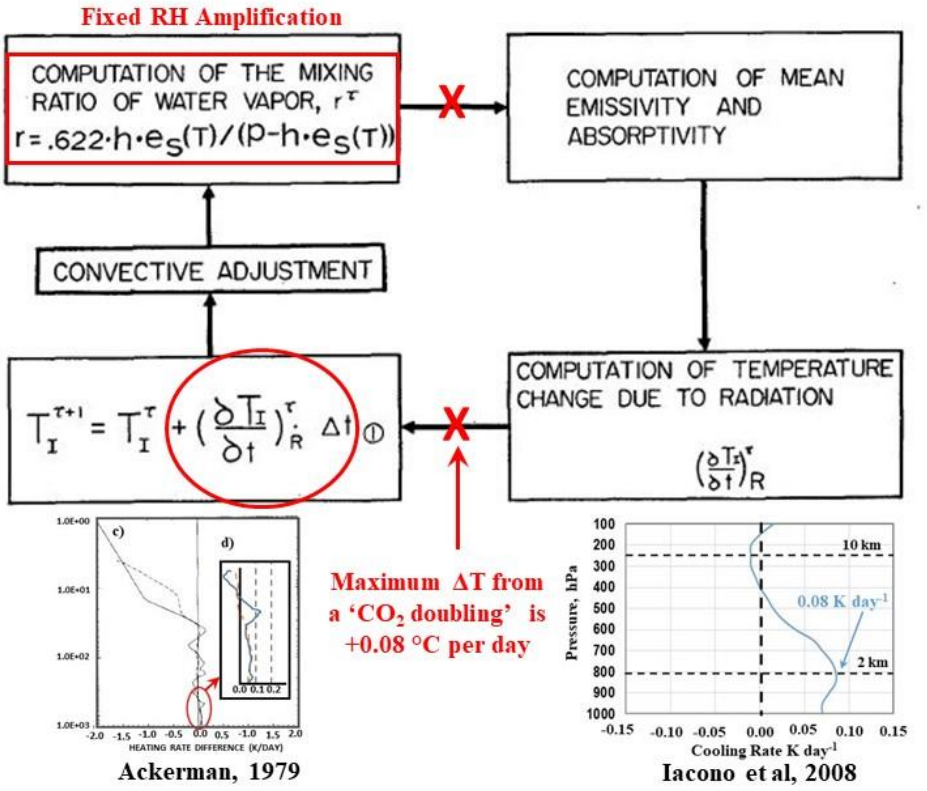

Fig. 2. Flow chart for the numerical integration

Figure 36: The time marching or integration procedure used in the MW67 model. When the CO_2 concentration is increased, the change in temperature for the integration is too small to detect in the real atmosphere and does not accumulate over time. In addition, there can be 'water vapor feedback'.

M&W used the same time integration procedure in MW75, so the increase in temperature produced by a doubling of the CO_2 concentration in their 'highly simplified' GCM is a mathematical artifact of the calculation. The model also required a year of model time to approach equilibrium. This is shown in Figure 37 (MW75 figures 5 and 3). H76 and H81 also used the invalid MW67 time marching algorithm.

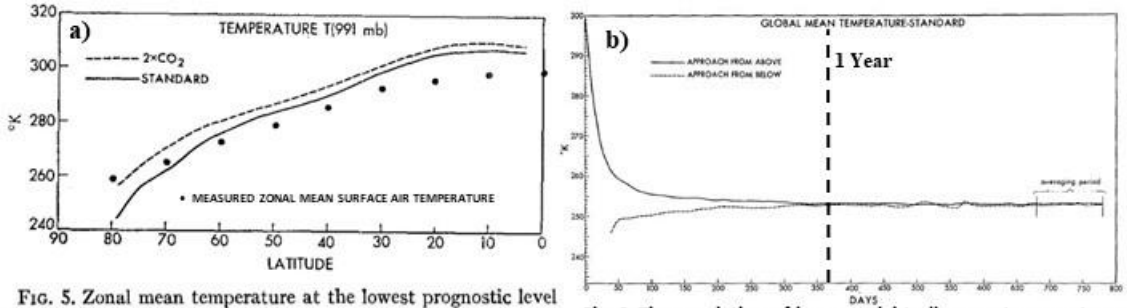

FIG. 5. Zonal mean temperature at the lowest prognostic level (i.e., ~991 mb). Dots indicate the observed distribution of zonal mean surface air temperature (Oort and Rasmusson, 1971).

Fig. 3. Time variation of (mass-weighted) mean temperature for the entire period of the two standard runs.

Figure 37: a) The mathematical artifacts generated by a 'CO_2 doubling' in MW75 and b) the time to reach model equilibrium.

Conclusions

The radiative transfer algorithms used in the MW67 model were quite good, considering the available spectroscopic data and the limited computer resources available in 1967. Unfortunately, M&W chose to use the equilibrium climate assumption and incorporated their radiative transfer algorithms into a steady state climate model. When the CO_2 concentration was increased in this model, the slight heating produced at each iteration in the model was allowed to accumulate and change the temperature. These mathematical artifacts were also amplified by the relative humidity assumption imposed on the air layers. The much larger diurnal and seasonal temperature changes were ignored. In the real atmosphere, these would overwhelm any 'CO_2 signal'. There was no attempt to validate the model temperature calculations using measured flux and temperature data even though such data were available, for example from the Great Plains Turbulence Field Program. The role of the oceans in setting the surface temperature and the coupling of the ocean surface temperatures to the weather station data through the daily convective transition temperature were never considered. The obvious time delays or phase shifts between the peak daily and seasonal solar insolation and the temperature response were ignored. M&W created the equilibrium climate fantasy land where climate modelers could play computer games and solve mathematical equations that had nothing to do with the earth's climate. The invalid time marching of integration procedure used in MW67 was also used in MW75, H76 and H81. These four papers provided the foundation of the climate fraud that continues today on a massive scale.

Acknowledgement

This work was performed as independent research by the author. It was not supported by any grant awards and none of the work was conducted as a part of employment duties for any employer. The views expressed are those of the author. He hopes that you will agree with them.

References

Normally, the references given in an article of this nature would be almost exclusively to the peer reviewed literature, with limited references to websites that provide access to climate data. Unfortunately, climate science has been thoroughly corrupted by the global warming fraud. The peer review process has collapsed and been replaced by blatant cronyism. Many of the publications in 'prestigious' journals such as Nature, Science, PNAS and others that relate to climate modeling predictions of global warming are fraudulent and should never have been published. Consequently, many of the important references given here are to website publications. This should not detract from the integrity of the information provided. Many of these website publications have received a more thorough review than they might have received through the traditional peer review process.

Ackerman, T. P. (1979), "On the effect of CO_2 on the atmospheric heating rates" *Tellus* **31** pp. 115-123. [https://a.tellusjournals.se/articles/10.3402/tellusa.v31i2.10416]

Arrhenius, S. (1896), "On the influence of carbonic acid in the air upon the temperature of the ground" *The London, Edinburgh, and Dublin Philosophical Magazine and Journal of Science* **41** pp. 237-276. [https://doi.org/10.1080/14786449608620846]

CERES (2004) [https://ceres.larc.nasa.gov/documents/press_releases/images/mnet.mp4] (Source: MyNASAData WebSite, Instrument: CERES/Terra, Release Date: 07/12/2004)

Clark, R. (2013), "A dynamic, coupled thermal reservoir approach to atmospheric energy transfer Part I: Concepts" *Energy and Environment* **24**(3, 4) pp. 319-340. [https://doi.org/10.1260/0958-305X.24.3-4.319]

"A dynamic, coupled thermal reservoir approach to atmospheric energy transfer Part II: Applications" *Energy and Environment* **24**(3, 4) pp. 341-359. [https://doi.org/10.1260/0958-305X.24.3-4.341]

Clark, R. and A. Rörsch, (2023) *Finding Simplicity in a Complex World - The Role of the Diurnal Temperature Cycle in Climate Energy Transfer and Climate Change*, Clark Rörsch Publications, Thousand Oaks, CA. Available from Amazon.

[https://www.amazon.com/dp/B0BZBPV32Q]

Further details and supplementary material are available at [https://clarkrorschpublication.com/index.html]

ENSO (2022), [https://psl.noaa.gov/gcos_wgsp/Timeseries/Data/nino34.long.data]

Eschenbach, W. (2010), "The thunderstorm thermostat hypothesis" *Energy and Environment* **21**(4) pp. 201-224. [https://doi.org/10.1260/0958-305X.21.4.201]

Feldman D.R., K. N. Liou, R. L. Shia and Y. L. Yung (2008), "On the information content of the thermal IR cooling rate profile from satellite instrument measurements" *J. Geophys. Res.* **113** D1118 pp. 1-14. [https://doi.org/10.1029/2007JD009041]

Fourier, J.-B. J. (1827), "Mémoire sur les températures du globe terrestre et des espaces planétaires" *Mém. Acad. R. Sci. Inst. Fr.*, **7** (1827) pp. 527-604. [https://www.academie-sciences.fr/pdf/dossiers/Fourier/Fourier_pdf/Mem1827_p569_604.pdf] English translation: [http://www.wmconnolley.org.uk/sci/fourier_1827/]

Fourier, J.-B. J. (1824), "Remarques générales sur les températures du globe terrestre et des espaces planétaires" *Annales de Chimie et de Physique* **27**, pp. 136–167. [https://gallica.bnf.fr/ark:/12148/bpt6k65708960/f142.image#] English translation: [http://fourier1824.geologist-1011.mobi/]

Fourier, J.-B. J. (1822), *Theorie analytique de la chaleur*, Didot, Paris.

[https://gallica.bnf.fr/ark:/12148/bpt6k29061r/f7.item]

Hale, G. M. and M. R. Querry (1973), "Optical constants of water in the 200 nm to 200 µm wavelength region" *Applied Optics*, **12**(3) pp. 555-563. [https://doi.org/10.1364/AO.12.000555]

Hansen, J., D. Johnson, A. Lacis, S. Lebedeff, P. Lee, D. Rind and G. Russell (1981), "Climate impact of increasing carbon dioxide" *Science* **213** pp. 957-956. [https://pubs.giss.nasa.gov/docs/1981/1981_Hansen_ha04600x.pdf]

Harde, H. (2017), "Radiation Transfer Calculations and Assessment of Global Warming by CO_2" *Int. J. Atmos. Sci.* 9251034 pp. 1-30. [https://doi.org/10.1155/2017/9251034]

Harper, K. C. (2004), "The Scandinavian tag team: Providers of atmospheric reality to numerical weather prediction efforts in the U. S. (1948-1955)" *Proc. Int. Commission on History of Meterology* **1.1** pp. 84-91. [https://journal.meteohistory.org/index.php/hom/issue/view/2]

Iacono, M. J., J. S. Delamere, E. J. Mlawer, M. W. Shephard, S. A. Clough, and W. D. Collins (2008), "Radiative forcing by long-lived greenhouse gases: Calculations with the AER radiative transfer models" *J. Geophys. Res.* **113**, D13103 pp. 1-8. [https://doi.org/10.1029/2008JD009944]

IPCC, *Climate Change 2021: The Physical Science Basis*. *Contribution of Working Group I to the Sixth Assessment Report of the Intergovernmental Panel on Climate Change* [Masson-Delmotte, V., P. Zhai, A. Pirani, S.L. Connors, C. Péan, S. Berger, N. Caud, Y. Chen, L. Goldfarb, M.I. Gomis, M. Huang, K. Leitzell, E. Lonnoy, J.B.R. Matthews, T.K. Maycock, T. Waterfield, O. Yelekçi, R. Yu, and B. Zhou (eds.)]. Cambridge University Press, Cambridge, United Kingdom and New York, NY, USA. (2021). In Press. doi:10.1017/9781009157896, [https://www.ipcc.ch/report/ar6/wg1/]

IPCC, *Climate Change 2013: The Physical Science Basis. Contribution of Working Group I to the Fifth Assessment Report of the Intergovernmental Panel on Climate Change* [Stocker, T.F., D. Qin, G.-K. Plattner, M. Tignor, S.K. Allen, J. Boschung, A. Nauels, Y. Xia, V. Bex and P.M. Midgley (eds.)]. Cambridge University Press, Cambridge, United Kingdom and New York, NY, USA, (2014)1535 pp. ISBN 9781107661820. [https://www.ipcc.ch/report/ar5/wg1/]

Kandel, R. and M. Viollier (2010), "Observation of the Earth's radiation budget from space" *Comptes Rendus Geoscience* **342**(4-5) pp. 286-300. [https://doi.org/10.1016/j.crte.2010.01.005]

Keeling (2023), *The Keeling Curve*. [https://scripps.ucsd.edu/programs/keelingcurve/]

Koll, D. D. B and T. W. Cronin (2018), "Earth's outgoing longwave radiation linear due to H_2O greenhouse effect" *PNAS*, **115**(41) pp. 10293-10298. [https://www.pnas.org/doi/10.1073/pnas.1809868115]

Lacis, A. A. and V. Oinas (1991), "A description of the correlated k distributing method for modeling nongray gaseous absorption, thermal emission and multiple scattering in vertically inhomogeneous atmospheres" *J. Geophys. Res.* **96**(D5) pp. 9027-9063. [https://doi.org/10.1029/90JD01945]

Lettau, H. H. and B. Davidson (1957a), *Exploring the Atmosphere's First Mile. Proceedings of the Great Plains Turbulence Field Program, 1 August to 8 September 1953* Volume I, Instrumentation and data evaluation, Oxford, Pergamon Press.

Available at:

[https://books.google.com/books/about/Exploring_the_Atmosphere_s_First_Mile.html?id=5bcJAQAAIAAJ]

Lettau, H.H. and B. Davidson (1957b), *Exploring the Atmosphere's First Mile. Proceedings of the Great Plains Turbulence Field Program, 1 August to 8 September 1953* Volume II, Site Description and Data Tabulation, Oxford, Pergamon Press.

Available at:

[https://books.google.com/books?hl=en&lr=&id=5bcJAQAAIAAJ&oi=fnd&pg=PA377&dq=Lettau,+H.H.+and+B.+Davidson,+Exploring+the+atmosphere%E2%80%99s+first+mile.+Oxford:+

Pergamon+Press,+1957.&ots=N0vbpjURx3&sig=sSTz9EMWpwi0XysXHTcWcLNxWv0#v=onepage&q&f=false]

Lorenz, E. N. (1973), "On the Existence of Extended Range Predictability" *J. Applied Meteorology and Climatology* **12**(3) pp. 543-546. [https://journals.ametsoc.org/view/journals/apme/12/3/1520-0450_1973_012_0543_oteoer_2_0_co_2.xml?tab_body=fulltext-display]

Lorenz, E.N. (1963), "Deterministic nonperiodic flow" *Journal of the Atmospheric Sciences* **20**(2) pp. 130-141. [https://journals.ametsoc.org/view/journals/atsc/20/2/1520-0469_1963_020_0130_dnf_2_0_co_2.xml]

Manabe, S. and F. Möller (1961) "On the radiative equilibrium and heat balance of the atmosphere" *Monthly Weather Review* **89**(12) pp. 503-532. [https://doi.org/10.1175/1520-0493(1961)089<0503:OTREAH>2.0.CO;2]

Manabe, S. and R. F. Strickler (1964) "Thermal Equilibrium of the Atmosphere with a Convective Adjustment" *J. Atmospheric Sciences* **21** pp. 361-385. [https://climate-dynamics.org/wp-content/uploads/2016/06/manabe64a.pdf]

Manabe, S. and R. T. Wetherald (1975) "The effects of doubling the CO_2 concentration in the climate of a general circulation model" *J. Atmos. Sci.* **32**(1) pp. 3-15. [https://journals.ametsoc.org/view/journals/atsc/32/1/1520-0469_1975_032_0003_teodtc_2_0_co_2.xml?tab_body=pdf]

Manabe, S. and R. T. Wetherald (1967) "Thermal equilibrium of the atmosphere with a given distribution of relative humidity" *J. Atmos. Sci.* **24** pp. 241-249. [http://www.gfdl.noaa.gov/bibliography/related_files/sm6701.pdf]

MODTRAN (2023), [https://climatemodels.uchicago.edu/modtran/modtran.doc.html]

NRL (2021), Naval Research Laboratory, HYCOM consortium for Data-Assimilative Ocean Modeling. [https://www7320.nrlssc.navy.mil/GLBhycomcice1-12/]

Oke T. R. (2006), *Initial guidance to obtain representative meteorological observations at urban sites* WMO/TD-No. 1250, World Meteorological Association, pp. 47.

[https://www.researchgate.net/publication/265347633_Initial_guidance_to_obtain_representative_meteorological_observations_at_urban_sites]

Plass, G. N. (1956) "The influence of the 15-micron carbon dioxide band on the atmospheric infrared cooling rate" *Quarterly Journal of the Royal Meteorological Society* **82** pp. 310-324. [https://doi.org/10.1002/qj.49708235307] available at [http://www.rescuethatfrog.com/wp-content/uploads/2017/02/Plass-1956c.pdf]

Pouillet, M. (1837), "Memoir on the solar heat, on the radiating and absorbing powers of the atmospheric air and on the temperature of space" in: *Scientific Memoirs selected from the Transactions of Foreign Academies of Science and Learned Societies*, edited by Richard Taylor, **4** pp. 44-90.

[http://nsdl.library.cornell.edu/websites/wiki/index.php/PALE_ClassicArticles/archives/classic_articles/issue1_global_warming/n2-Poulliet_1837corrected.pdf]

Original publication: (1836), "Mémoire sur la chaleur solaire: sur les pouvoirs rayonnants et absorbants de l'air atmosphérique et sur la température de l'espace" *Comptes Rendus des Séances de l'Académie des Sciences*, Paris. 7, pp. 24-65.

Ramaswamy, V., W. Collins, J. Haywood, J. Lean, N. Mahowald, G. Myhre, V. Naik, K. P. Shine, B. Soden, G. Stenchikov and T. Storelvmo (2019), "Radiative Forcing of Climate: The Historical Evolution of the Radiative Forcing Concept, the Forcing Agents and their Quantification, and Applications" *Meteorological Monographs* Volume **59** Chapter 14. [https://doi.org/10.1175/AMSMONOGRAPHS-D-19-0001.1]

SOI (2022), [http://www.bom.gov.au/climate/enso/soi_monthly.txt]

TRITON (2021), [https://www.pmel.noaa.gov/tao/drupal/disdel/]

Tyndall, J., (1861) "On the Absorption and Radiation of Heat by Gases and Vapours, and on the Physical Connexion of Radiation, Absorption, and Conduction" *Philosophical Transactions of the Royal Society of London* **151** pp. 1-36. [https://royalsocietypublishing.org/doi/pdf/10.1098/rstl.1861.0001]

Tyndall, J. (1863), "On radiation through the Earth's atmosphere" *Proc. Roy Inst.* Jan 23 pp. 200-206.

UAH (2022), [https://www.nsstc.uah.edu/data/msu/v6.0/tlt/uahncdc_lt_6.0.txt]

Vasavada, A. R., J. L. Bandfield, B. T. Greenhagen, P. O. Hayne, M. A. Siegler, J-P Williams and D. A. Paige (2012), "Lunar equatorial surface temperatures and regolith properties from the Diviner Lunar Radiometer Experiment" *J. Geophys. Res.* **117** E00H18 pp. 1-12. [https://doi.org/10.1029/2011JE003987]

Wang, W. C., Y. L. Yung, A. A. Lacis, T. Mo and J. E. Hansen (1976), "Greenhouse effects due to man-made perturbations of trace gases" *Science* **194** pp. 685-690. [https://pubs.giss.nasa.gov/docs/1976/1976_Wang_wa07100z.pdf]

Williams, J.-P., D. A. Paige, B. T. Greenhagen and E. Sefton-Nash (2017), "The global surface temperatures of the Moon as measured by the Diviner Lunar Radiometer Experiment" *Icarus*, **283** pp. 300-325. [https://doi.org/10.1016/j.icarus.2016.08.012]

WRCC, (2022), [https://wrcc.dri.edu/sod/arch/hbF.html]

Wijngaarden, W. A. van and W. Happer (2022), "IR Forcing by Greenhouse Gases" CO_2 Coalition Publication 6/10/22, [https://co2coalition.org/wp-content/uploads/2022/03/Infrared-Forcing-by-Greenhouse-Gases-2019-Revised-3-7-2022.pdf]

Yu, L., X. Jin, and R.A. Weller (Jan. 2008), *Multidecade global flux datasets from the objectively analyzed air-sea fluxes (OAFlux) project: latent and sensible heat fluxes, ocean evaporation, and related surface meteorological variables* OAFlux project technical report OA-2008-01. [http://apdrc.soest.hawaii.edu/doc/OAFlux_TechReport_3rd_release.pdf]